

**SILICON-ON-INSULATOR OPTICAL
WAVEGUIDES AND WAVEGUIDE DEVICES**

A THESIS

**SUBMITTED TO THE DEPARTMENT OF PHYSICS
AND THE INSTITUTE OF ENGINEERING AND SCIENCE
OF BILKENT UNIVERSITY
IN PARTIAL FULFILLMENT OF THE REQUIREMENTS
FOR THE DEGREE OF
MASTER OF SCIENCE**

**By
İsa Kiyat
September 2000**

**QC
661
.K59
2000**

SILICON-ON-INSULATOR OPTICAL WAVEGUIDES AND WAVEGUIDE DEVICES

A THESIS

SUBMITTED TO THE DEPARTMENT OF PHYSICS
AND THE INSTITUTE OF ENGINEERING AND SCIENCE
OF BILKENT UNIVERSITY
IN PARTIAL FULFILLMENT OF THE REQUIREMENTS
FOR THE DEGREE OF
MASTER OF SCIENCE

By

İsa Kiyat

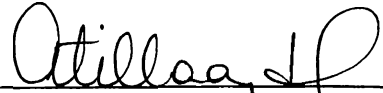
September 2000

DC
661
-K59

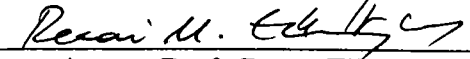
2000

RD 53293


I certify that I have read this thesis and that in my opinion it is fully adequate, in scope and in quality, as a dissertation for the degree of Master of Science.


Prof. Atilla Aydın (Supervisor)


I certify that I have read this thesis and that in my opinion it is fully adequate, in scope and in quality, as a dissertation for the degree of Master of Science.


Assoc. Prof. Recai Elialtıođlu

I certify that I have read this thesis and that in my opinion it is fully adequate, in scope and in quality, as a dissertation for the degree of Master of Science.


Asst. Prof. Serdar Özçelik

Approved for the Institute of Engineering and Science:


Prof. Mehmet Baray,
Director of Institute of Engineering and Science

Abstract

SILICON-ON-INSULATOR OPTICAL WAVEGUIDES AND WAVEGUIDE DEVICES

İsa Kiyat

M. S. in Physics

Supervisor: Prof. Atilla Aydınlı

September 2000

Silicon-on-insulator(SOI) optical waveguides, directional couplers and some types of MMI couplers were designed, fabricated and characterized at a wavelength of $1.55 \mu\text{m}$. Effective index method and the single mode condition for rib waveguide was used in design of optical waveguides. BPM simulations were extensively employed for all fabricated devices. Waveguides and the other devices were defined on SOI material by wet chemical etching in KOH solutions. Fabricated devices were characterized on a standard fiber optic measurement setup with a DFB laser as its IR light source. In characterization of optical waveguides the single mode condition was verified and insertion loss was measured to be 12.2 dB for TE and 12.7 dB for TM polarized light as the best values. Furthermore, the propagation loss found to be 0.70 dB/cm for TE and 0.76 dB/cm for TM which is typical . Characterized directional couplers gave results completely consistent with their BPM simulations. 1x2, 2x2, 1x4 and 1x8 type MMI couplers were also found to gave expected behaviors. Splitting ratios as low as 0 dB and 0.55 dB was measured.

Keywords: Integrated optics, silicon-on-insulator(SOI), optical waveguide, single mode condition, BPM, optical loss, butt coupling, anisotropic KOH etching, directional coupler, multimode interference(MMI), MMI coupler.

Özet

YALITKAN ÜSTÜ SİLİSYUMA DAYALI OPTİK DALGA KILAVUZLARI VE DALGA KILAVUZUNA DAYALI AYGITLAR

İsa Kiyat

Fizik Yüksek Lisans

Tez Yöneticisi: Prof. Atilla Aydınlı

Eylül 2000

Yalıtkan üstü silisyuma dayalı dalga kılavuzları, doğrusal çiftleyiciler ve bazı çeşit çok kipli girişim çiftleyicilerinin tasarımı, üretimi ve $1.55 \mu\text{m}$ dalga boyunda karakterizasyonu yapıldı. Optik dalga kılavuzlarının tasarımında etkin indis yöntemi ve sırt dalga kılavuzları için tekil kip koşulu bağıntısı kullanıldı. Ayrıca, BPM simülasyonları yoğun olarak kullanıldı. Dalga kılavuzları ve diğer aygıtlar KOH çözeltisi içinde izotropik olmayan ıslak aşındırma yöntemiyle oluşturuldu. Üretilen cihazlar, DFB kızıl ötesi lazer kaynağı olan standart bir fiber optik ölçüm düzeneğinde karakterize edildi. Optik dalga kılavuzu karakterizasyonunda tekil kip şartı teyit edildi ve optik giriş kaybı TE polarize ışık için en iyi değerler 12.2 dB ve TM polarize ışık için 12.7 dB olarak ölçüldü. Ayrıca optik iletim kaybı da TE için 0.70 dB/cm ve TM için 0.76 dB/cm olarak bulundu. Karakterize edilen doğrusal çiftleyiciler BPM simülasyonlarıyla tamamen tutarlı sonuçlar verdi. Ayrıca, 1x2 ve 2x2 çok kipli girişim çiftleyicilerin de beklenen özellikler gösterdiği tespit edildi. 0 dB ve 0.55 dB kadar küçük ayrılma oranları ölçüldü.

Anahtar

sözcükler: Tümleşik optik, yalıtkan üstü silisyum, optik dalga kılavuzu, tekil kip şartı, BPM, optik kayıp, uçuca çiftleme, izotropik olmayan KOH aşındırması, doğrusal çiftleyici, çok kipli girişim, çok kipli girişim çiftleyicisi.

Acknowledgement

I would like to express my deepest gratitude to *Prof. Dr. Atilla Aydınk* for his supervision during research, encouragement and friendly understanding throughout this thesis work. I would like thank Alpan Bek for all his help during the early stage of this work.

I would like also thank Murat Gure, Gungur Sincer and all the other ARL people for their help in making ARL a good research environment.

My many thanks are to Özgür Çakır, Emre Tepedelenliođlu, Feridun Ay, M. Ali Can, Selim Tanrıseven, Kerim Savran, Kamil Erkan, Sefa Dađ, İbrahim Kimukin and Mehmet Bayındır for being what a friend should be and their moral support.

I would like to dedicate this thesis to my family who have given continuous support throughout my life and Evla for her love and support throughout this work.

This work is supported by TUBİTAK Grant # 199E006.

Contents

Abstract	i
Özet	iii
Acknowledgement	v
Contents	vi
List of Figures	viii
List of Tables	xi
1 Introduction	1
1.1 Integrated Optics	2
1.2 Silicon and Silicon-on-insulator (SOI) in Integrated Optics	4
2 Theoretical Considerations	9
2.1 Analysis of Optical Waveguide	10
2.2 Single Mode Waveguide and Single Mode Condition	17
2.3 Loss in Optical Waveguides	22
2.3.1 Optical Waveguide Loss Mechanisms	23
2.3.2 Measurement of Optical Waveguide Losses	24
2.4 Optical Waveguide Directional Couplers	27
2.5 Optical Multi-Mode Interference(MMI) Couplers	32
2.5.1 Important Issues in Design and Characterization	36

3	Material Properties and Device Fabrication	39
3.1	SOI Structure and Wafer Fabrication Techniques	39
3.2	Sample Preparation	43
3.2.1	Sample Cleaning	43
3.2.2	Masking Material Deposition	44
3.3	Photolithography; Pattern Transfer	46
3.4	Anisotropic KÓH etching	48
4	Measurements and Characterization	58
4.1	Thickness Measurement Results of SOI Wafers Used	58
4.2	Characterization of SOI Optical Single Mode Waveguides	62
4.2.1	Measurement Setup	62
4.2.2	Verification of Single Mode Condition	64
4.2.3	Optical Waveguide Loss Measurement	68
4.3	Characterization of Optical Directional Couplers	73
4.4	Characterization of Optical MMI Couplers	78
4.4.1	The Mask Design	79
4.4.2	Measurements and Results	80
4.4.3	Discussions	88
5	Conclusions and Discussions	90

List of Figures

2.1	Slab Waveguide Structure	10
2.2	The Light rays in a slab waveguide; for confined (a) and not confined(b) light.	12
2.3	TE and TM polarizations in slab waveguide	12
2.4	A schematic of light in the slab waveguide as waves and rays.	15
2.5	TE modes in a SOI slab waveguide with thickness of 1 μm	16
2.6	Types of rectangular dielectric waveguides	18
2.7	EIM analysis of a rib waveguide	19
2.8	Single Mode Condition for rib waveguides with H=3,4and 5 μm	22
2.9	Schematic layout of a directional coupler	28
2.10	Cross section of a rib waveguide directional coupler(a) and its EIM counterpart(b)	29
2.11	The power exchange between waveguide A and B	31
2.12	Some MMI coupler examples	32
2.13	Lateral modes in a multimode waveguide with metal(a) and semiconductor(b) walls	33
3.1	A picture of SOI structure	40
3.2	Process layout of BESOI and <i>smart – cut</i> technologies	42
3.3	PECVD reactor structure	45
3.4	Effect of the waveguide strip orientation on the waveguide profiles on (100) surface	49
3.5	SEM photograph of the initial etching results; waveguide profile	50
3.6	SEM photograph of the initial etching results; surface	50

3.7	SEM photograph of the etching results at 40 °C ; surface and waveguide walls	51
3.8	The etching results at 35 °C; surface and waveguide walls.	52
3.9	The etching results at 30 °C; surface and waveguide walls.	52
3.10	SEM photograph of a cross section of a SOI waveguide fabricated by KOH etching.	53
3.11	A top view photograph of SOI directional couplers fabricated by KOH etching; the lines closer to each other are straight waveguide sections.	53
3.12	Top view photographs of input and output ports of SOI MMI couplers fabricated by KOH etching.	54
3.13	SEM photograph of a bad (not optically cleaved) waveguide facet.	55
3.14	Photograph of optically cleaved waveguide facets.	56
3.15	All steps in fabrication of SOI optical waveguides.	57
4.1	A slice taken from a wafer for layer thickness measurement.	59
4.2	SEM photographs of layers taken at (a) 0.8 mm and (b) 39 mm to the wafer edge for Wafer 2.	60
4.3	Measured layer thicknesses for Wafer 1.	60
4.4	Measured layer thicknesses for Wafer 2.	61
4.5	BPM simulations of optical power confinement for a SOI rib waveguide of different SiO ₂ layer thicknesses.	61
4.6	DFB laser wavelength peak value variation with laser temperature.	62
4.7	Optical measurement setup.	64
4.8	Transverse fundamental and first excited mode profiles of a SOI SM (a) and MM (b) waveguide structure computed using BPM.	65
4.9	Comparison of BPM simulation results (b) with SM condition results(a).	66
4.10	TE and TM fundamental modes of a single mode waveguide on sample SMSOI09.	68
4.11	Output images of an output port of SOI waveguides on sample SOIMMI05 with different alignments.	69

4.12 Slopped rib facets after a standard optical quality cleavage.	70
4.13 Measured insertion losses versus waveguide length.	72
4.14 Output images and peak profiles at different straight section lengths(L).	75
4.15 Coupling ratios and fitting curves for the characterized couplers. .	76
4.16 BPM simulation results of straight sections only: <i>XZ</i> counterparts and coupling ratios for both TE and TM, $L=4250 \mu\text{m}$	77
4.17 BPM simulation results, s-bends included: <i>XZ</i> counterpart and coupling ratios for TE and $L=1250 \mu\text{m}$	78
4.18 BPM simulation results for 1x2 MMI power splitters and 2x2 MMI couplers.	81
4.19 BPM simulation results for 1x4 and 1x8 MMI power splitters. . .	82
4.20 Output port images of 1x2 MMI power splitters for various MMI section lengths	84
4.21 Measured splitting ratio versus MMI section length for 1x2 devices of $48 \mu\text{m}$ width.	85
4.22 Output port images of 2x2 MMI couplers for various MMI section lengths	86
4.23 Measured splitting ratio versus MMI section length for 2x2 MMI couplers of $36 \mu\text{m}$ width.	87
4.24 Measured splitting ratio versus MMI section length for 2x2 MMI couplers of $64 \mu\text{m}$ width.	87
4.25 Output port images of 1x8 and 1x4 MMI power splitters for various MMI section lengths	88

List of Tables

1.1	Optically active and passive materials for OIC	3
3.1	The recipe file parameters used for deposition of Si_3N_4 , masking film.	46
4.1	The thicknesses of SOI wafers used.	58
4.2	The geometrical dimensions of analyzed SOI optical waveguides. .	67
4.3	Typical measured insertion losses.	71
4.4	Geometrical dimensions of the characterized directional couplers .	73
4.5	List of MMI structures on the designed mask.	80

Chapter 1

Introduction

"Knowledge is Power", has said one ad campaign, a simple, clear and self explained statement. Instead, if we are asked "Is Knowledge Power?", most of us would say "Of course!".

Information and its distilled form, knowledge, is gaining more importance in our lives day by day. It is nearly impossible to imagine that we live without computers, televisions, satellites, undersea fiber networks, cellular phones, fax machines, printers, and all other devices used to produce, transfer, manipulate and access information.

The electronic devices, mainly the mass produced high density semiconductor devices have played the important role in the modern information age. The information processing speed is the most remarkable feature of these devices. Are the electronic devices the only solution for the information age? To answer this question, the demands of the information age on candidate devices and technologies must be well understood, which are met by the electronic devices to some extent. These demands may be stated as the following,¹ information reception (detection), information enhancement(amplification), information manipulation, memory, information transfer, information generation, and information display. We know from the advances in the last few decades that there is an alternative technology named *integrated optics* -exploiting light-and/or *integrated optoelectronics* -exploiting both light and electrons.

1.1 Integrated Optics

Instead of cables, the metal interconnects and integrated electronic circuits in the integrated electronics, light guiding optical fiber, dielectric waveguides and optical integrated circuits (OIC) are utilized in integrated optics, respectively. Integrated optics showed great progress in meeting the demands of information age since 1960's, with the development of the laser as a stable source of coherent light.² References⁽³⁾ and ⁽⁴⁾ are very good sources for a historical overview of integrated optics.

There are some points where integrated optic devices (optical fibers and OIC's) have advantages over electronic devices. Electronic devices have limitations on the inter-connectivity due to metal interconnects, difficulties in transmission of information over long distances -integrated optics has showed the most significant development in this area by using optical fiber networks-, external electromagnetic interference effects, small bandwidth, comparatively large size and heavy weight and scattering of electrons as they move in a material. Being totally different from the above criteria, no phase information could be kept in a system of electronic devices after some amount of distance. This does not bring any functional problem for the electronics devices, actually. However, this is a point where integrated optics will find new horizons. That is, capability of keeping phase information of light leads the emergence of new so-called "future" devices in integrated optics which are based on "interference effect".

Two forms of optical integrated circuits are widely used, *hybrid* OIC's in which two or more substrate materials are bonded together and *monolithic* OIC's in which a single substrate material is used for all components of the circuit. Since nearly all OIC's need a light source, i.e. a laser, monolithic OIC's can only be fabricated in optically *active* materials, that is, materials with direct bandgaps and capable of light generation. The materials that are incapable of light generation are optically *passive*. Both optically passive and active materials commonly used in fabrication of integrated circuits are presented in Table. 1.1.

The most commonly used material in monolithic OIC's is the gallium

PASSIVE	ACTIVE
Quartz	Gallium arsenide
Lithium niobate	Gallium aluminium arsenide
Lithium tantalate	Gallium arsenide phosphide
Tantalum pentoxide	Gallium indium arsenide
Niobium pentoxide	Other III-V semiconductors with direct bandgaps
Silicon	Other II-VI semiconductors with direct bandgaps
Polymers	

Table 1.1: Optically active and passive materials for OIC

aluminum arsenide, $Ga_{1-x}Al_xAs$ or the gallium indium arsenide phosphide $Ga_xIn_{1-x}As_{1-y}P_y$. One of the most important properties of these optically active materials is that by changing the fractional atomic concentration of the constituents, the emitted wavelengths can be varied from $0.65 \mu m$ (for AlAs) to $1.7 \mu m$ (for GaInAs). The other important properties which deserve to be mentioned are the following: firstly, these materials are transparent for wavelength range of $0.6 \mu m$ to $12 \mu m$ and have relatively large electro optic and acoustooptic properties. Then, the nearly equal lattice constants of GaAs and AlAs (5.646 and 5.369 \AA , respectively)⁵ makes epitaxial growth of layers of $Ga_{1-x}Al_xAs$ with greatly different Al concentration possible with minimal interfacial strain being introduced. Finally, they are the cheapest of all III-V and II-VI materials, due to their widespread use. These materials are used in fabrication of all type OIC's components, but especially preferred for the fabrication of multilayered heterojunction lasers.

Lithium niobate, $LiNbO_3$ is an anisotropic material with high electrooptic and acousto-optical coefficients. It is transparent for the range of $0.2 \mu m$ to $12 \mu m$. $LiNbO_3$ based hybrid OIC's are the most commercialized integrated optic systems. Nearly all of the integrated optic devices first realized on $LiNbO_3$ except lasers and detectors. Apart from these properties it has a very high birefringence which makes it a good material for polarization sensitive devices.^{2,6} Another optically passive materials group is polymers which represents a huge class of

materials. Among them, polycarbonate which used for compact discs and PMMA (photoresist) are used for purely passive optical components.⁶ Other polymers exhibit a large electro-optical or nonlinear coefficient, but at the expense of a poor long term stability. Silicon, which is also optically passive, based technologies are mentioned in the next section.

Optical waveguides are one of the building blocks of integrated optic technology. Waveguides have been realized in different types and geometries planar, circular, rib, ridge, buried etc. In both optically passive and active materials including those briefly explained here. The loss characterization is the key step when analyzing a waveguide. The losses of as large as 2-5 dB/cm for GaAlAs systems, 0.5 dB/cm for $LiNbO_3$, and 0.1 dB/cm for silicon based optical waveguides are typical.⁷ Apart from being fabricated and analyzed as a separate devices, optical waveguides are passive components of most of the integrated optical devices, e.g. in directional couplers, multimode interference couplers, modulators, Mach-Zehnder type devices, access components of detectors and lasers in OIC's, etc.

1.2 Silicon and Silicon-on-insulator (SOI) in Integrated Optics

Integrated optics on silicon has received great attention especially in the last decade. A very clear reason may come to mind immediately. That is, since silicon is the most commonly used material in semiconductor electronics, it is commercially available in high quality and at low prices. Hence, it is natural to investigate silicon as a candidate platform for integrated optics. But, why to have waited until late 1980's. The answer hide in the latest developments in silicon materials technology⁸ (other than bulk silicon), first with the emergence of silicon-on-insulator(SOI) as a platform for both OIC's and electronic integrated circuits (e.g. VLSI, CMOS, etc.), second epitaxial growth of silicon based alloys with tailored optical properties (SiGe-heterostructures) and doped silicon. There

are some other technologies such as silica on silicon and siliconoxynitride(SiON) films. However, they use silicon only as substrate material.

Plasma enhanced chemical vapor deposition (PECVD) or flame hydrolysis(FHD) techniques are used to deposit silica layers on silicon or quartz substrates. Then the substrates are heated to about $1000\text{ }^{\circ}\text{C}$ to make glass layers transparent. These silica layers are designed such that refractive index differences of 0.5-1.5 percent are possible. This flexibility is useful for different applications. That is low refractive index difference is good for low loss devices whereas, high refractive index difference allows fabrication of bend-waveguides with smaller radii. The typical waveguide losses in this technology ranges from 0.01 dB/cm for low refractive index difference and large core sizes to 0.07 dB/cm for high refractive index and small core sizes.⁹ On the other hand, in SiON technology, SiON layers with refractive indices between 1.45 (silicon-oxide refractive index) and 2 (silicon-nitride refractive index) are deposited by optimized PECVD or LPCVD techniques on an already deposited thermal silicon-oxide layer on a silicon substrate. Light guides in the SiON layer which has a slightly larger refractive index than lower cladding (thermal oxide) and upper cladding (silicon-oxide deposited after waveguide fabrication). Before waveguide or device fabrication the deposited SiON layers are annealed at an approximate temperature of $1140\text{ }^{\circ}\text{C}$. This step is needed to remove N-H bonds which exist in deposited SiON layers. These bonds cause an infrared absorption and its first overtone is found at 1510 nm which is very near to the optical communication wavelengths, 1550 nm . The typical losses for SiON based waveguide technology are 0.1 dB/cm for slab waveguides and 0.2 dB/cm for channel waveguides. One of the most important advantages of the SiON technology with respect to weakly guiding materials technologies is that waveguide bend radius as small as 1.5 mm are possible due to the high refractive index difference between SiON layer and its cladding.¹⁰

In doped epitaxial silicon based waveguides, guiding is obtained if the doping level of the epilayer is lower than the doping level of the substrate. However, these waveguides suffer from high optical losses, waveguide losses in the range of

15-20 dB/cm have been measured for rib waveguides with epilayers of thickness between $7\mu m \leq H \leq 43\mu m$ and doping levels of a few $10^{14}cm^{-3}$ for epilayer and $10^{18} - 10^{19} cm^{-3}$ for substrate.¹¹ These high losses may be further decreased by using larger H and a very highly doped substrate, because the main source of the loss is the substrate absorption. Applying the above statement the optical losses as low as 1.2-1.5 dB/cm have been achieved.¹²

Si-Ge heterostructures can be fabricated by both MBE¹³ or CVD-growth.^{14,32} Germanium ($n \simeq 4.3$) is used to slightly increase the refractive index of silicon ($n \simeq 3.5$). For a resultant $Si_{1-x}Ge_x$ -alloy, $n_{SiGe} \approx n_{Si} + 0.3x + 0.32x^2$ gives refractive index which is enough for weakly guiding structures. Due to the similar lattice constants of Si and Ge which both are belong to group IV of the periodic table, epitaxial growth of thin strained SiGe-layers is possible. Waveguides on MBE-grown strained $Si_{0.99}Ge_{0.01}$ layer have been fabricated with losses 3-5 dB/cm at $\lambda = 1.3\mu m$ ¹³ and with reduced loss of 0.6 dB/cm on CVD-grown $Si_{1-x}Ge_x$ layers.¹⁶ The high cost and difficulty in growing of SiGe by MBE and CVD, lead indiffusing of germanium into commercially available silicon. SiGe is a good platform for photodetector fabrication and these devices have been integrated with SOI waveguides.¹⁷ So SiGe is an important material due to its compatibility with SOI technology. Most of the integrated optical components and devices have been realized on the materials mentioned here, we do not attempt to include all these information here which would be a lengthy task.

Among these silicon based materials, SOI -apart from its promises in future electronic integrated circuits- has very unique optical properties due to its very unique structure. It uses pure silicon as its guiding layer and has a large refractive index difference between silicon ($n \simeq 3.5$ and $SiO_2(n \simeq 1.45)$). Silicon has very good optical properties at the optical telecommunication bandwidth (around $1.3\mu m$ and $1.55\mu m$) and it is fully compatible with silicon electronic integrated circuit. Since, full replacement of integrated electronics with integrated optics will probably not happen for a very long time, this compatibility is one of SOI OIC's most important advantages over other technologies.

SOI integrated optics technology has developed very rapidly, because it raises

on the well-established silicon integrated electronics micromachining technology. So there is nearly no need to establish a new device fabrication technologies. Like bulk silicon SOI is now commercially available both at high quality and at relatively low prices. Although, there are a number of fabrication techniques of SOI substrate, only two of them has good material properties and have succeeded in becoming commercial, namely Separation by IMplemented OXYgen (SIMOX) technology and Bond-and-Etchback (BE-SOI) technology,¹⁸ more information on these SOI fabrication techniques are given in section 3.1.

In last decade optical properties of SOI waveguides have been investigated and a number of both passive and active(based on electrooptic effect) optical integrated devices on SOI developed. The fabrication techniques are not presented here , they are explained in Chapter 3 extensively. Waveguides on SOI was first realized with relatively high propagation losses then by means of advanced fabrication techniques this value come to 1 dB/cm , and then to 0.5 dB/cm , and finally to 0.1 dB/cm using large cross-section SOI rib waveguides.¹⁹⁻²³ Typically, the losses around 0.5 dB/cm are obtained provided that silicon top layer is larger than 4 μm and waveguides are designed to be single mode. Also the dependence of propagation loss on the thickness of insulator (SiO_2) has been investigated.²⁴

Apart from optical waveguides, a number of SOI guided wave optical devices and circuits (SOI-OIC's) have also been demonstrated. Some examples are integrated 3 dB directional couplers with excess insertion loss (that is chip loss) of 1.9 dB ,²⁵ 5x9 star couplers with loss of 1.3 dB ,²⁶ asymmetric Mach-Zehnder type wavelength filters with -18 dB crosstalk²⁷ and waveguide interferometers based on electrooptic effect²⁸(low electrooptic response of the silicon enhanced by ion implantation), optical switches based on thermo-optic effect^{29,30} with 5 μs rise time and 150 mW switching power³⁰ and low-loss multimode couplers.⁸

The ultimate purpose of this effort of which this work is only the first part, is the development of a library of low-loss silicon-on-insulator (SOI) optoelectronic devices. To reach this goal, SOI waveguides(singe and multimode), directional couplers and MMI couplers have been designed, simulated, fabricated and characterized to some extend so far. This thesis work summarizes

the fundamental physical theories behind these optical integrated devices in Chapter2, describes the each fabrication step in Chapter3 and explains the measurements and presents results in Chapter4.

Chapter 2

Theoretical Considerations

As was stated earlier, the optical waveguide being the integrated optics counterpart of the metallic interconnects in integrated electronics, is the fundamental component of optical integrated circuits. So it is necessary to analyze the optical waveguide before we try to study optical integrated devices. In this chapter, the slab waveguide and single mode waveguide at the beginning and is discussed first, then optical directional couplers and multimode interference (MMI) couplers are treated.

Light propagates in an optical waveguide in the so-called optical modes according to wave optics. In its simplest meaning, like its counterparts in many other physical situations, modes are the different "ways" of propagation of optical energy in a waveguide. These modes, can be differentiated from each other by spatial distribution of optical energy in the waveguide, the propagation constant and the orientation of electric and magnetic fields (polarization) of the each mode. An optical waveguide can support a definite number of modes at a specific wavelength, the waveguide is called a single mode waveguide if only one mode is supported, and a multimode waveguide if more than one mode is supported. The number of modes for an optical waveguide is determined by its refractive index distribution, that is the refractive index values of materials making up the waveguide, and the waveguide geometrical dimensions.

Wave optics is the most important tool of the integrated optics but not

the only. Ray optics (geometric optics) which assumes that light travels in straight lines, is also useful in analyzing the optical waveguide. Ray optics is used whenever it is applicable and it is an approximation of the wave optics in the limit of small wavelengths and/or large waveguide or device dimensions, especially when the waveguides are multimoded.

Since we mainly deal with single mode waveguides which are very small in dimensions, wave optics will be used in most of the following sections. A brief summary of ray optics will also be given since the planar (slab waveguide) optical waveguide, which is the first step in understanding of the waveguide theory, can also be analyzed by ray optics.

2.1 Analysis of Optical Waveguide

Being the simplest of waveguides, it is logical to analyze the slab waveguide first. Slab waveguides are very good models for studying more general types of optical waveguides. Slab waveguides are dielectric slab films.

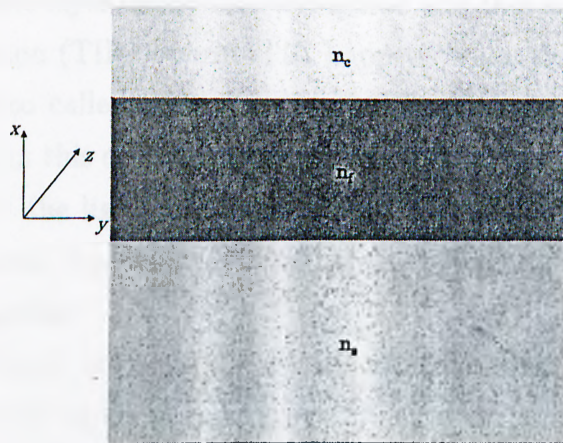


Figure 2.1: Slab Waveguide Structure

As is seen in Fig. 2.1, in general, it has a minimum of three different layers. For guidance of light, n_f (refractive index of guiding film) must be larger than n_c (refractive index of cladding layer) and n_s (refractive index of substrate layer),

$$n_f > n_s \geq n_c. \quad (2.1)$$

When $n_s = n_c$, the slab waveguide is said to be *symmetric* and *antisymmetric* otherwise, $n_s \neq n_c$. So the symmetric waveguides are special cases of antisymmetric ones.

Since, the slab waveguide is an optical waveguide, all the rules apply to it. The slab waveguide supports a definite number of optical modes, and at least one if it is symmetric. These modes can be found by applying the boundary conditions to Maxwell's equations. However, the same modes for slab waveguides can be found by using ray optics concepts which has a relatively easier procedure.

In ray optics, it is assumed that a light ray in a homogeneous optical medium follows straight paths. Light changes its path after passing from one medium to another with different refractive index, and the paths in different media have a relation between them through the well known Snell's law. The Snell's law relates the angles with respect to the normal to a dielectric interface that a beam forms when passing through the interface. For guiding of light, rays should be confined in the middle layer of the slab waveguide and this is only possible when total internal reflection (TIR) occurs. TIR happens when the angle of incidence is smaller than the so called critical angle of TIR. Light rays having angles of incidence smaller than this critical angle will be confined (see Fig.2.2). When the phase information of the light rays having multiple reflections on the interfaces is brought into picture, it is seen the only light rays which are incident at some specific angles are guided.

On the other hand, in wave optics, all analysis start with solving well known Maxwell equations for a source free ($\rho=0$, $\vec{J}=0$), linear (ϵ and μ are independent of \vec{E} and \vec{H}) and isotropic medium. Maxwell equations are strongly coupled. They can be decoupled through a standard procedure of creating a single second order differential equation. This procedure when applied to the Maxwell equations leads to

$$\nabla^2 \psi - \mu\epsilon \frac{\partial^2 \psi}{\partial t^2} = 0 \quad (2.2)$$

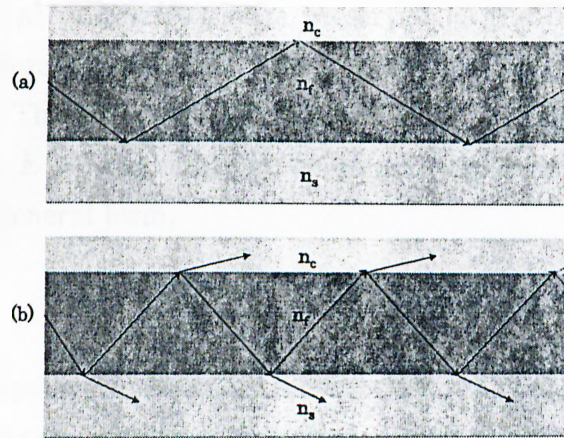


Figure 2.2: The Light rays in a slab waveguide; for confined (a) and not confined(b) light.

the wave equation and ψ stands for either of \vec{E} or \vec{H} .

Now we can solve, the wave equation for the slab waveguide in Fig. 2.1. The parameters are chosen such that $n_f > n_s > n_c$ and the guiding layer has thickness h . To make the problem simpler, rectangular cartesian coordinate system can be utilized. z is always chosen to show propagation direction. There are two cases emerging from geometry, either \vec{E} or \vec{H} is parallel to the layer interfaces, which define either TE or TM polarizations respectively as shown in Fig.2.3.

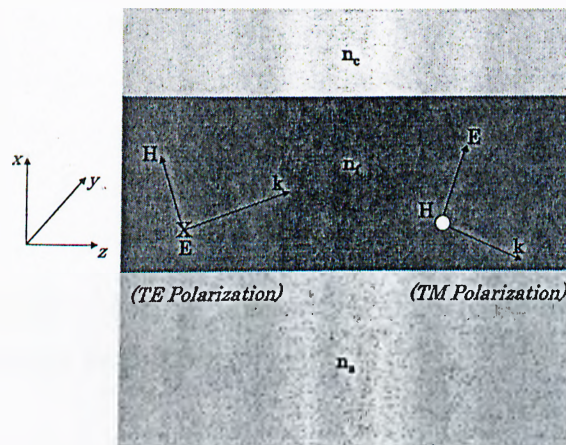


Figure 2.3: TE and TM polarizations in slab waveguide

Also, TE and TM polarizations are preserved as the light propagates in z direction and undergoes reflections with respect to the rectangular cartesian coordinate system. The analysis will be done for TE, and can be similarly done for TM. In TE case, \vec{E} only has E_y component and the electromagnetic radiation have the following general form,

$$\vec{E}(x, y, z, t) = \vec{E}(x, y)e^{i(\omega t - \beta z)} \quad (2.3)$$

where β is the propagation constant in z direction. It is also called the longitudinal wavevector. ω is the angular frequency given in terms of c , the speed of light and λ , the wavelength of electromagnetic wave as,

$$\omega = \frac{2\pi c}{\lambda} \quad (2.4)$$

Then the wave equation, Eqn. 2.2 for E_y can be written as scalar wave equation:

$$\nabla^2 E_y + k_0^2 n^2(x) E_y = 0 \quad (2.5)$$

here $n(x)$ is given as

$$n(x) = \begin{cases} n_s & x < -h \\ n_f & 0 > x > -h \\ n_c & x > 0 \end{cases} \quad (2.6)$$

and k_0 as

$$k_0 = \frac{2\pi}{\lambda} \quad (2.7)$$

E_y has no y dependence, since the slab waveguide is infinite in y direction. So, E_y can be written using Eqn. 2.3 as

$$E_y(x, z) = E_y(x)e^{-i\beta z} \quad (2.8)$$

Substitution of Eqn. 2.8 into the scalar wave equation (Eqn. 2.5), gives

$$\frac{\partial^2 E_y(x)}{\partial x^2} + (k_0^2 n^2(x) - \beta^2) E_y = 0 \quad (2.9)$$

The solution to the Eqn. 2.9 changes according to sign of the value inside the parenthesis. The cases are,

$$E_y(x) = E_0 e^{\pm \sqrt{\beta^2 - k_0^2 n^2} x} \quad \text{if } \beta > k_0 n \quad (2.10)$$

and

$$E_y(x) = E_0 e^{\pm \sqrt{k_0^2 n^2 - \beta^2} x} \quad \text{if } \beta < k_0 n \quad (2.11)$$

where E_0 is the field amplitude at $x=0$. The solution given in Eqn. 2.10 has a real exponential form and to be physically meaningful the solution with minus sign is chosen, which leads to a negatively decaying solution. The other case gives an oscillating solution. Two new coefficients are defined which are useful to understand the physical processes in the two cases. They are

$$\begin{array}{ll} \text{Attenuation Coefficient, } \gamma = \sqrt{\beta^2 - k_0^2 n^2} & \text{if } \beta > k_0 n \\ \text{Transverse Wavevector, } \kappa = \sqrt{k_0^2 n^2 - \beta^2} & \text{if } \beta < k_0 n \end{array} \quad (2.12)$$

The two cases are visually compared in Fig.2.4 according to both ray optic and wave optic approaches.

As seen clearly in the Fig. 2.1, for guidance or total internal reflection to take place, the condition of the Eqn. 2.1 can be restated as

$$k_0 n_s < \beta < k_0 n_f \quad (2.13)$$

Then the general solution of E_y for the slab waveguide can be written in either oscillatory or decaying waves according to Eqn. 2.13,

$$\begin{array}{ll} E_y = A e^{-\gamma_c x} & x > 0 \\ E_y = B \cos(\kappa_f x) + C \sin(\kappa_f x) & -h < x < 0 \\ E_y = D e^{\gamma_s(x+h)} & x < -h \end{array} \quad (2.14)$$

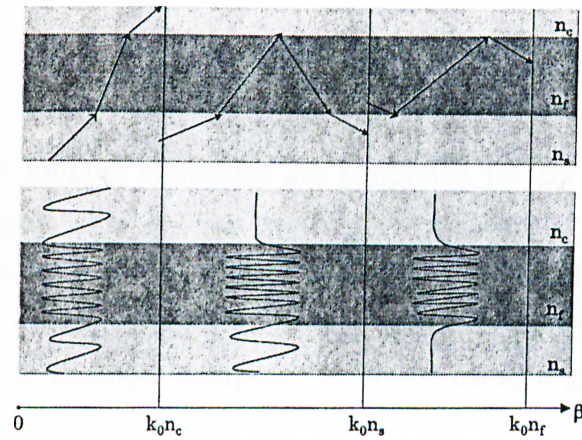


Figure 2.4: A schematic of light in the slab waveguide as waves and rays.

where the coefficients A , B , C and D will be determined from boundary conditions. There are two boundary conditions to be satisfied. Tangential E and H must be continuous at the interfaces. The first condition says E_y will be continuous. Utilizing Maxwell equations and the constitutive relations to find an expression for the continuity of the tangential H results in

$$H_z = \frac{i}{\mu\omega} \frac{\partial E_y}{\partial x} \quad (2.15)$$

Applying these conditions will give us the coefficients in Eqn. 2.14, but instead we will find a more fundamental relation. After a few manipulations and applying the boundary conditions gives the so called *the eigenvalue equation* for β for TE polarization.

$$\tan(h\kappa_f) = \frac{\gamma_c + \gamma_s}{\kappa_f \left[1 - \frac{\gamma_c \gamma_s}{\kappa_f^2}\right]} \quad (2.16)$$

The above equation is also called the characteristic equation of TE modes of a slab waveguide. Eqn. 2.16 is a transcendental equation and it can only be solved numerically or graphically.

Setting the problem for TM case and using the same procedure yields a relation, Eqn. 2.17, which is somewhat different;

$$\tan(h\kappa_f) = \frac{\kappa_f \left[\frac{n_f^2}{n_s^2} \gamma_s + \frac{n_f^2}{n_c^2} \gamma_c \right]}{\kappa_f^2 - \frac{n_f^4}{n_c^2 n_s^2} \gamma_c \gamma_s} \quad (2.17)$$

These complex looking equations are simplified for the special case of the symmetric waveguide. The eigenvalues of these eigenvalue equations, β_{TE} and β_{TM} can be found for a slab waveguide with a definite thickness h and index values for its layers using either a numerical or graphical software in a personal computer. A simple example computation result using a graphical software is given in Fig.2.5.

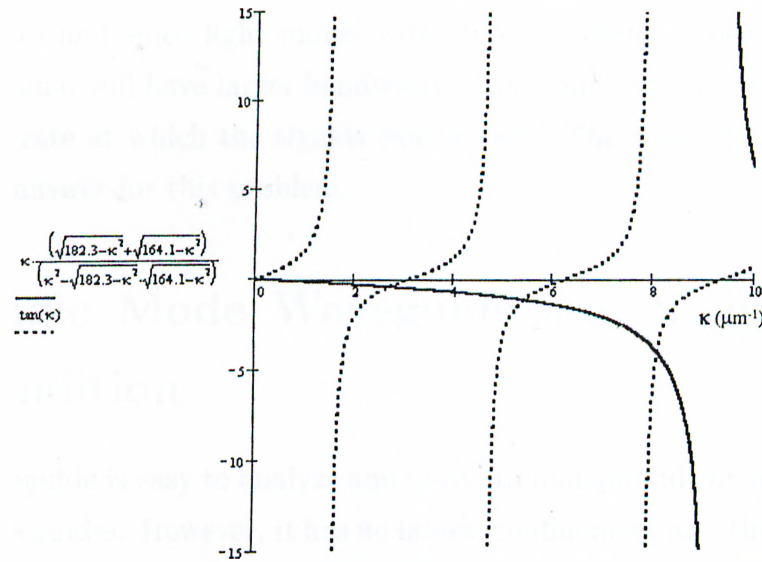


Figure 2.5: TE modes in a SOI slab waveguide with thickness of 1 μm .

As seen in the example given in Fig.2.5 the waveguide confines a definite number of modes. This corresponds to existence of a definite number of eigenvalues of eigenvalue equation for β , and a definite number of light rays traveling at different angles in the waveguide.

The number of modes, m , can be determined after plotting the eigenvalue equation, the number of nodes are equal to the number of modes supported, but there is a simple approximate formula as well:

$$m = \text{Int}\left[\frac{hk(n_f^2 - n_s^2)^{1/2}}{\pi}\right] \quad (2.18)$$

This is an approximation only and in general good, when m is large. This equation gives important results. The number of modes that a waveguide confines increases as the difference between the refractive index of the guiding film and the substrate and the thickness of the film, h , increase. The numerator in the Eq. 2.18 is called the normalized frequency of the waveguide. This value is generally used to designate a waveguide. The number of modes is a key concept in design of waveguides and waveguide devices. If a signal with a narrow bandwidth is launched to a waveguide with m larger than one, the signal will be distributed over all modes and since light moves with slightly different speeds in different modes, the signal will have larger bandwidth after some distance. This effect will decrease the rate at which the signals can be sent. The single mode waveguide comes as an answer for this problem.

2.2 Single Mode Waveguide and Single Mode Condition

The slab waveguide is easy to analyze and useful to understand the basic concepts of optical waveguides. However, it has no lateral confinement and this reduces the number of applications where it can be used. The alternatives are circular fibers and dielectric rectangular waveguides. The fibers are not compatible with planar processing technology, such as planar chips, which are backbones of integrated electronics. The slab waveguide can be laterally confined and resulting structure is the so called dielectric rectangular waveguide. The rectangular waveguides may have several geometric shapes to establish the lateral confinement namely, rib waveguide (Fig.2.6a), ridge waveguide (Fig.2.6b), channel waveguide (Fig.2.6c) and diffused waveguide (Fig.2.6d). Rib and ridge waveguides have the same shape, that is the top dielectric layer has a rib, the difference between them is that the guiding layer in ridge waveguide is the layer under the rib layer whereas

the rib layer functions as the guiding layer for rib waveguides.

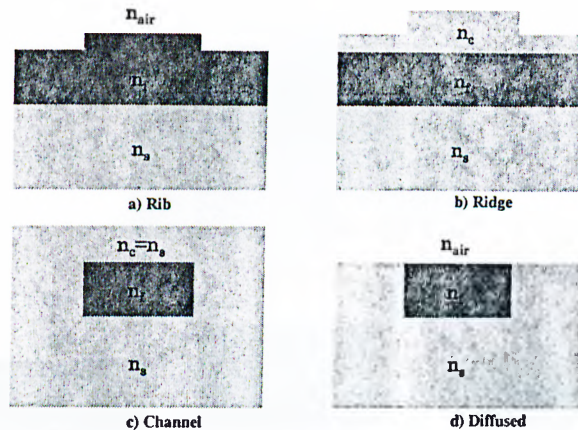


Figure 2.6: Types of rectangular dielectric waveguides

The SOI optical waveguide we designed, fabricated and characterized in this work is a very good example of the rib waveguide type. The mode analysis of the rectangular waveguides (i.e.: of the SOI waveguide) is a bit cumbersome and exact analytical solutions can not be so easily found, instead, some simplified analytical results based on the solution of the wave equation are further corrected by some perturbation techniques. What is actually needed are some simple methods which will be useful for design purposes. There are two waveguide design tools, namely effective index method (EIM), which is an relatively easy method to apply and useful for most of the design purposes and the beam propagation method (BPM), which is a numerical simulation method and not an approximation to the analytical solution. The SOI rib single mode waveguides were designed applying EIM, then BPM were also used for verification.

A rectangular waveguide can be analyzed in two dimensions (x and y) as seen in Fig.2.7. The effective index method comes into picture at this point, it divides the 2D problem into two 1D problems (slab waveguides for which the exact solutions are straightforward).

In this method the rib waveguide is divided so that three slab structures are formed as seen in Fig.2.7. The propagation constant, β , for the guiding mode of interest and wavelength are calculated from the eigenmode equations of the

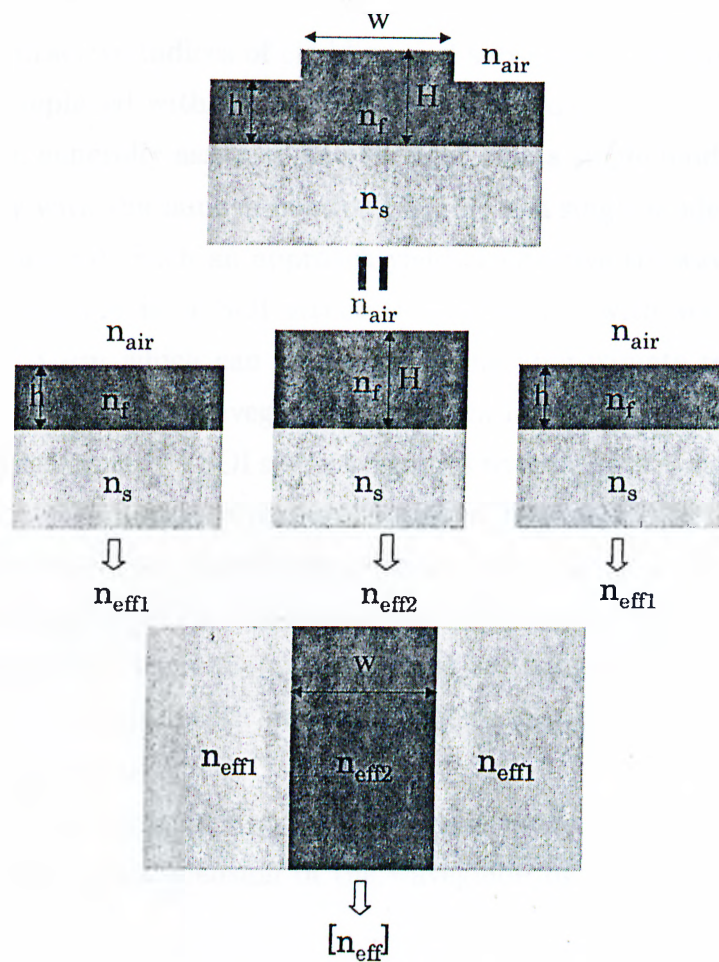


Figure 2.7: EIM analysis of a rib waveguide

slab waveguide for the two slab waveguide structures. Then the effective indices (n_{eff1} and n_{eff2}) are calculated for each structure using,

$$n_{eff} = \frac{\beta}{k_0} \quad (2.19)$$

Then, using these effective indices an artificial slab waveguide structure is formed as in Fig.2.7 and calculation of the β is repeated for this structure using Eqn. 2.19. The resulting effective index is the effective index of the original rib waveguide,

also. It should be noted that in solving the eigenvalue equation for the artificial slab waveguide structure which has n_{eff2} as the guiding film refractive index and n_{eff1} as the refractive indices of cladding and substrate, the initial polarization of the light is replaced with its orthogonal counterpart.

It had been generally assumed and thought that a single mode rib waveguide is possible only with the same dimension (height) as a single mode slab waveguide of the same material. Such an approach yields ineffective rib waveguides. Single mode slab waveguide in a SOI structure is obtained with waveguide heights smaller than $0.3 \mu m$ which can be verified using approximate relation given in Eq. 2.18. So, any SOI slab waveguide with height larger than this value would be multimode, in reference⁽³¹⁾ SOI slab waveguides with heights ranging between 0.5 and $2 \mu m$ were examined experimentally and all were found to be multimoded. Rib waveguides with such small dimension would result in high coupling losses between the waveguide and a single mode fiber which have dimension of $9 \mu m$. On the other hand, at the beginning of the 90's, it has been shown that single mode rib waveguides are possible with large cross section that is dimensions comparable with that of single mode fibers.³²

For the rib waveguide in Fig.2.7, *the single mode condition* which relates vertical and horizontal dimension of the waveguide by facilitating EIM can be stated as

$$t < c + \frac{r}{\sqrt{1-r^2}} \quad (2.20)$$

for

$$r > 0.5 \quad (2.21)$$

where

$$t = \frac{\omega_{eff}}{H_{eff}} \quad r = \frac{h_{eff}}{H_{eff}}$$

$$h_{eff} = h + q \quad H_{eff} = H + q$$

$$\omega_{eff} = \omega + \frac{2\gamma_c}{k\sqrt{n_f^2 - n_c^2}} \quad q = \frac{\gamma_c}{k\sqrt{n_f^2 - n_c^2}} + \frac{2\gamma_c}{k\sqrt{n_f^2 - n_s^2}}$$

and

$$\begin{aligned} \gamma_{c,s} &= 1 && \text{for } TE \text{ modes} \\ \gamma_{c,s} &= \left(\frac{n_{c,s}}{n_f}\right)^2 && \text{for } TM \text{ modes} \end{aligned} \quad (2.22)$$

The relation in Eq. 2.20 leads to single mode propagation in horizontal (lateral) direction while Eq. 2.21 ensures propagation of only one mode in vertical (transverse) direction by avoiding deep etching of the waveguide. The constant c is given as 0.3 in the reference ⁽³²⁾ which was found from an approximation to a BPM numerical solution. However, it has been recently stated that c values of 0 or -0.05 give better single mode condition for rib waveguide design purposes.³³ These latter constants put more restriction on the single mode condition and ensures realization single mode waveguides in fabrication.

Using single mode conditions given above is not very practical when fabricating waveguides. So, we have reorganized the relations for definite rib heights, H , which is fixed with the silicon top layer for the SOI structure and obtained a plot of controlled fabrication parameters, waveguide width, w and etch depth, e (see Fig.2.8). These are the H values of the SOI structures we used in realization of the devices presented in this work. The areas remained under the plot lines defines the single mode region and the rest remains as multimode region, also due to Eq. 2.21, etch depths can not exceed half of the H values.

Actually, the rib waveguide treatment can be made more realistic by considering the sloped walls formed during chemical wet etching. In this treatment, the sloped edges can be approximated by a staircase function of definite number of stairs, and the eigenvalue equation is solved and cut off widths are calculated by the help of an computer program,³⁴ in an effectively long and complex manner. Our SOI waveguides are also fabricated by an wet etch process which yields sloped walls of 54.7° , but we prefer to use the EIM analysis explained above, due to its reasonable accuracy and practical simplicity. The single mode

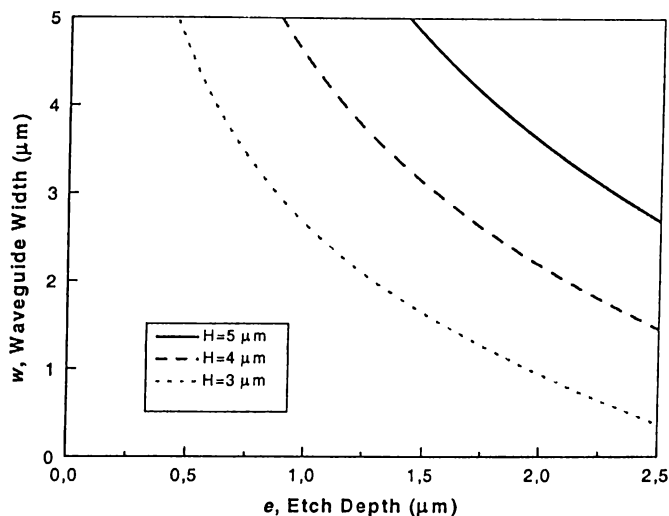


Figure 2.8: Single Mode Condition for rib waveguides with $H=3,4$ and $5 \mu m$.

condition will be compared with the BPM simulations and experimental results in Chapter 4.

2.3 Loss in Optical Waveguides

Integrated optical devices are designed to have low power consumption, high speed, size compatibility, low cost, and *low loss*. Low loss or low attenuation may be the most important concept among all. Characterizing a waveguide means loss measurement after mode analysis of the waveguide. Light reduces in power as it propagates in the waveguide. Power decrease is due to several mechanisms. Power loss in a waveguide is expressed in terms of dB/cm where dB is defined as;

$$Power(dB) = 10 \log_{10} \left(\frac{P_{in}}{P_{out}} \right) \quad (2.23)$$

The well known definition, 3dB means $P_{out} = 0.5P_{in}$ and so on.

2.3.1 Optical Waveguide Loss Mechanisms

Scattering Losses

Two types of scattering losses are under consideration, volume scattering and surface scattering. The former, volume scattering, depends on the number and relative size of imperfections in waveguide material with respect to light wavelength. These imperfections are voids, crystalline defects and contaminant atoms. These imperfections are generally smaller than the wavelength and smaller in number, so volume scattering is not a main scattering mechanism for SOI optical waveguides.

Surface scattering can be an important source of loss and should be reduced during fabrication. Since, light reflects many times from surfaces of a waveguide, it has been showed quantitatively that the surface scattering loss depends on ratio of the roughness of the waveguide surfaces to the wavelength directly, and the waveguide thickness and the amount of the tail of the evanescent field. In the case of the SOI rib waveguides the roughness of the buried SiO₂ layer, the thickness variation of the top silicon layer and the roughness of the walls of the etched rib are the points to be considered. The first two are related with the fabrication of the SOI substrate and they are results of the optimized commercial technologies. The last is related with the etching of silicon during fabrication process, which was our first task to deal with.

Absorption Losses

This is a mechanism which is mainly important for semiconductor waveguides and is no so important in amorphous thin films and in crystalline ferroelectric materials. Band edge absorption and free carrier absorption are the two types of absorption loss mechanisms that are dominant in semiconductor waveguides like SOI waveguides.

Photons with energy greater than the bandgap energy is absorbed in semiconductors, and the energy of the photon leads valence electrons to be excited to the conduction band. This is a very strong effect. Silicon has a indirect band

gap with 1.1 eV ($0.9 \mu\text{m}$ in wavelength). So, we do not have to worry about this loss mechanisms since the wavelength employed in the telecommunication are 1.3 and $1.55 \mu\text{m}$, well apart from the band gap of the silicon.

Free carrier absorption is intraband absorption. A photon gives its energy to an electron in the conduction band exciting it to a higher energy level. This effect is strong when the number of free carriers (electrons and holes) is large. This absorption can be eliminated by utilizing substrates with low doping levels. Low doping levels means small number of free carriers and this means high resistivity. We eliminate this effect for SOI waveguide using wafers with silicon top layers having high resistivity.

Radiation Losses

Actually, the scattering loss is also a radiation loss, that is guided light is somehow leaked into either substrate or cladding and not guided anymore. However, radiation loss is the loss taking place when the waveguide design is near or beyond cutoff. Well confined single mode waveguides do not suffer significantly from this loss mechanism. However, it is important for multimode waveguides and bending waveguides. In case of SOI rib waveguides, radiation losses are not so significant as long as the waveguide is designed as a single mode waveguide away from the cutoff and the input light is well coupled into the waveguide facet so that slab modes would not be excited.

2.3.2 Measurement of Optical Waveguide Losses

To measure the loss, the simple and straightforward way is to input some light with known optical power into the one facet of the waveguide and measure the optical power at the other facet of the waveguide. Some problems arise when this method is applied. First of all this is not an efficient way for the loss measurement of slab and other multimode waveguides, since individual mode losses can not be determined by this method. Prism-coupling loss measurement technique is preferred for multimode waveguides since it allows measurement of loss for each

mode.² Another problem is that the losses at the input and output ports during coupling can not be known exactly. Despite its drawbacks, this technique is used for determination of losses in single mode waveguides. There are two ways of applying this technique called end-fire coupling (and/or butt-coupling) and Fabry-Parot resonance techniques which are explained below.

End-Fire and Butt Coupling

In *end – fire coupling* technique, which is the simplest of all, the light with a known wavelength and optical power is focused into cleaved or polished input face of a waveguide using a microscope objective and the transmitted power is measured at the output port. This measurement is repeated for a large number of waveguides having different lengths, but otherwise identical. This task is accomplished by starting measurements with a relatively long (e.g. several millimeters) waveguide sample then repetitively shortening the sample by cleaving, or cutting and polishing and measuring these new waveguides with different lengths. The most important problem of this technique is with alignment which should be optimized for each waveguide - microscope objective pair by maximizing output optical power. Then the logarithm of relative transmission is plotted with respect to waveguide length. The plot is a straight line and its slope gives loss coefficient. This technique is effective for the single mode waveguides which can be easily cleaved to optical quality.

Instead of focusing light by a microscope objective an optical single mode fiber can be butt coupled into the waveguide face. The technique is called *butt coupling* in this case. End-fire coupling is better than butt coupling because alignment can be easier and better optimized by focusing light with an microscope objective into waveguide facet than directly butt coupling an optical single mode fiber of diameter nearly $9 \mu m$ to a waveguide facet of size about $3 \times 3 \mu m^2$. All the other procedures for measurement and data analysis are the same for both techniques.

Fabry-Perot Interferometer

If the waveguide for which the loss to be measured has optically cleaved facets, it can be considered as a microscopic Fabry-Perot interferometer with facets as the partially transmitted mirrors of the interferometer. Interference pattern is constructed when the phase of the propagating light in the Fabry-Perot interferometer is changed. Optical phase change in a waveguide can be accomplished in two ways, by either increasing waveguide sample temperature by a few degrees or changing the wavelength of the input light continuously. The second way is relatively easier if a temperature tuned distributed feedback (DFB) laser is used. When applying this technique the same setup as in the end-fire coupling technique is used, except the output of the detector should be visualized graphically to identify the minimums and maximums of the fringes. An oscilloscope or an computer connected optical powermeter or even multimeter would help.

The ratio of the maximum transmitted optical intensity to minimum intensity can be defined as

$$\frac{I_{max}}{I_{min}} = \frac{(1 + Re^{-\alpha L})^2}{(1 - Re^{-\alpha L})^2} \quad (2.24)$$

in terms of the facet reflectance, R , loss coefficient, α and waveguide (Fabry-Perot cavity) length, L . Defining this ratio as κ , the loss coefficient can be stated as

$$\alpha = \frac{1}{L} \ln \left[R \frac{\sqrt{\kappa} + 1}{\sqrt{\kappa} - 1} \right] \quad (2.25)$$

Using the Eq. 2.25, the optical loss for a waveguide can be determined in one measurement if the facet reflectance is known. In practice the same optical quality can not be repeated in each cleavage of a waveguide sample so the reflectance of the facets can not be known exactly. In that case, the same procedure applied in end-fire coupling technique can be employed here. That is, measuring maximum and minimum intensity for waveguide samples with the same features except different lengths. Then, $10 \log[(1 + \sqrt{\kappa})/(1 - \sqrt{\kappa})]$ which has dimension of dB, versus waveguide length is plotted. This plot will be a straight line. The slope

gives optical loss coefficient and extrapolated value to $L=0$ defines reflectivity of facets.

These techniques can be utilized in optical single mode waveguide loss characterization as long as their limits are considered. Fabry-Perot interferometer technique should be preferred if the waveguides can be cleaved to optical quality. Since it gives directly the total losses explained in this section earlier. This total loss is called *propagation loss*. The end-fire coupling gives a loss value in which the so-called *insertion loss* is included. The insertion loss arises from the mismatch between waveguide modes and the light at both input and output ports. This loss has nothing to do with the waveguide material or fabrication quality and it depends on the size of the waveguide, quality of cleaving or polishing and the optimization of the alignment. In the literature end-fire and butt coupling have been reported to be used in SOI waveguide loss characterization mainly.

2.4 Optical Waveguide Directional Couplers

Optical tunneling is responsible for the coupling of optical power from one waveguide to an other one. The device composed of this pair of waveguides is called a waveguide coupler in general and *directional coupler* if the power exchange happens in a coherent fashion so that the direction of propagation does not change. Directional couplers are one of the fundamental waveguide devices used in integrated optic circuits. They have been used in circuits designed for power splitting, modulation or switching of light signals, wavelength filtering and polarization selecting.

A directional coupler consists of two identical waveguides very closely placed, as in Fig.2.9. The light incident at input of one of the waveguides couples to the other as it propagates and full coupling of the optical power is possible for long enough coupling length.

In integrated optics, coupled mode formalism is used to treat directional couplers. Coupled mode theory is the theory describing the power exchange between all the optical modes. What happens when coupling occurs is that the

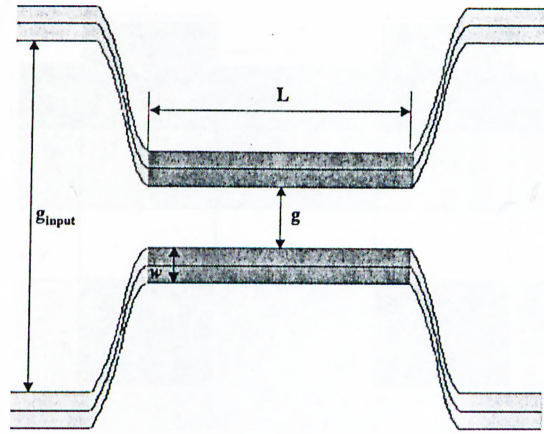


Figure 2.9: Schematic layout of a directional coupler

electromagnetic field of waveguides in a directional coupler is not ideal anymore when there is light propagating in adjacent waveguide. Rather it is perturbed by the evanescent tail of the adjacent waveguide. The coupled mode theory describes this perturbed field by superposition of unperturbed or ideal modes of the waveguide. The basic coupled mode theory is based on the scalar wave equation. The advanced couple mode theories based on vector wave equation is still a developing topic. What is computed at the end is coupling coefficient, κ , for a definite directional coupler design. Knowing κ , the exact coupling length can be determined.

We will demonstrate the coupled mode theory approach for a directional coupler with rib waveguide structure, but the results can be applied to directional couplers with other rectangular waveguide structures by only replacing the refractive indices shown in Fig.2.10 with appropriate ones for each.

This coupled mode approach is also known as *degenerate mode coupling*, since both waveguides(A and B in Fig.2.10) have the same transverse and longitudinal wavevectors, κ_x , κ_y and propagation constant, β . The electric fields in waveguide A and B are

$$E_A(x, y, z) = A \cos(\kappa_y y + \phi_y) \cos(\kappa_x/2(x + (w + g)))e^{-i\beta z} \quad (2.26)$$

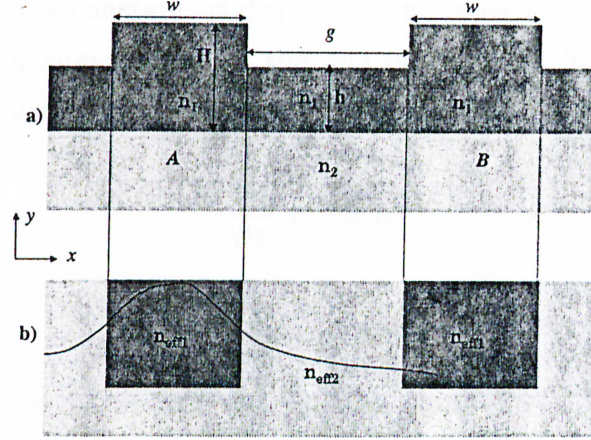


Figure 2.10: Cross section of a rib waveguide directional coupler(a) and its EIM counterpart(b)

$$E_B(x, y, z) = B \cos(\kappa_y y + \phi_y) \cos(\kappa_x/2(x - (w + g)))e^{-i\beta z} \quad (2.27)$$

Now, the perturbation made by the evanescent tail of the mode of waveguide A in waveguide B, which is called *polarization perturbation*, can be written as

$$\begin{aligned} P_{pert}(x, y, z) &= \epsilon_0(n_{eff1}^2(x, y) - n_{eff2}^2)E_A(x, y) \\ &= \left[\frac{A}{2}\epsilon_A(x, y)e^{-i\beta z - \omega t} + c.c. \right] \end{aligned} \quad (2.28)$$

Only the modes in the same direction will couple to each other, that is there will be no coupling to the backward mode of the waveguide B. Therefore, the amplitude equation of motion will be given in terms of forward mode of B as

$$\begin{aligned} -\frac{\partial B}{\partial z}e^{-i\beta z - \omega t} + c.c. &= -\frac{i}{2\omega} \frac{\partial^2}{\partial t^2} \int_S \epsilon_B(x, y)P_{pert}dS \\ &= \frac{i\omega}{2} \int_{-\infty}^{\infty} \epsilon_0(n_{eff1}^2(x, y) - n_{eff2}^2)\epsilon_B(x, y) \\ &\quad \left\{ \frac{A}{2}\epsilon_B e^{-i\beta z - \omega t} + c.c. \right\} dx dy \\ &= i\kappa A e^{-i\beta z - \omega t} + c.c. \end{aligned} \quad (2.29)$$

where κ , the coupling constant, is defined by the integrals and all the constants. There is also a relation similar to the one in Eq. 2.29 for the coupling from waveguide B to waveguide A. These both relations reduces to

$$\frac{\partial A}{\partial z} = -i\kappa B \quad (2.30)$$

$$\frac{\partial B}{\partial z} = -i\kappa A \quad (2.31)$$

since exponential terms cancel out for the same β 's. These are strongly coupled differential equations and must be solved simultaneously. Substitution of derivative of Eq. 2.30 into Eq. 2.31 results in

$$\frac{\partial^2 A}{\partial z^2} = -\kappa^2 A \quad (2.32)$$

a second order differential equation, which can be easily solved for initial conditions, $A(0) = 1$ and $B(0) = 0$ to give

$$\begin{aligned} A(z) &= \cos(\kappa z) \\ B(z) &= -i \sin(\kappa z) \end{aligned} \quad (2.33)$$

As seen in Fig.2.11, the total power goes back and forth between two waveguides and the driven field (waveguide B) always lags 90° . Using the results in Fig.2.11 gives L as

$$L = \frac{\pi}{2\kappa} + \frac{q\pi}{\kappa} \quad (2.34)$$

then complete energy transfer happens if q is integer, and the length for $q=0$ is called *coupling length* and represented by L_c . q values other than integers produce couplings between 0 and 100 percent. κ and L_c strongly depends on g , the gap between waveguide pairs, w , the width of waveguides H , the waveguide (rib) height, h , the waveguide slab height and the refractive index difference between guiding layer and substrate.

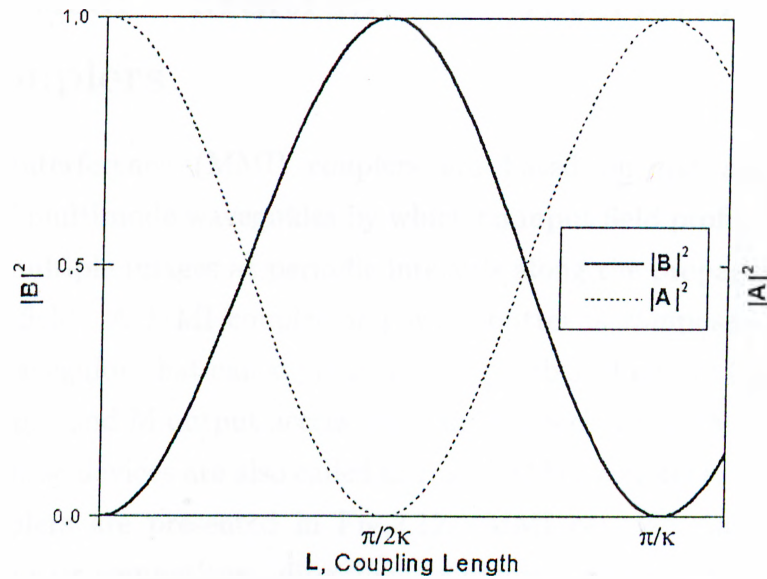


Figure 2.11: The power exchange between waveguide A and B

Coupled mode formalism is not practical when a directional coupler is designed. As can be seen in the Fig.2.9, waveguides must be bend apart to decouple them at the output. As practical coupling also takes place in this region they bring further complexity to the analysis. They cause radiation loss(as stated in previous section) and change the effective coupling constant and L_c . For this reasons beam propagation method(BPM) has been used in our directional coupler analysis. A commercial BPM based computer program, named *BeamProp* has been used to simulate directional couplers. An available mask design was applied to some SOI single mode waveguide structures, then coupling lengths were deduced from these simulations. Simulation results will be given along with optical measurement of fabricated couplers in Chapter4.

2.5 Optical Multi-Mode Interference(MMI) Couplers

Multimode interference (MMI) couplers are based on *the self – imaging property*³⁵ of multimode waveguides by which an input field profile is reproduced in single or multiple images at periodic intervals along the propagation direction of the input field. A MMI coupler or power splitter is composed of an central multimode waveguide that can support a large number of modes (typically larger than 3), N input and M output access waveguides which are usually singlemoded. This is why these devices are also called as $N \times M$ MMI couplers. Some examples of MMI couplers are presented in Fig.2.12. MMI couplers have been strong alternatives for its competitors, directional couplers, adiabatic X and Y junction splitters and diffractive star couplers with their high tolerance to polarization and wavelength variations(high bandwidth), acceptable fabrication tolerance, low access losses and ability to split light to ports of any number.

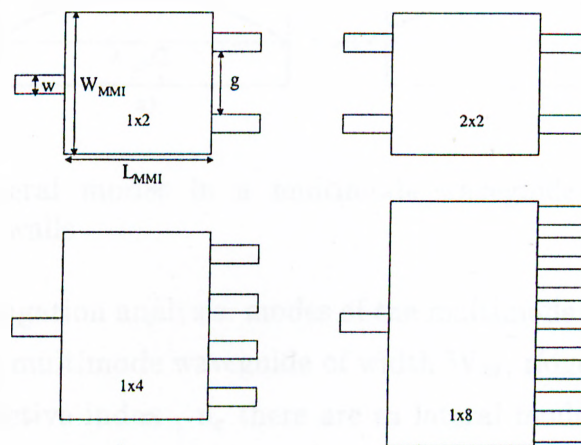


Figure 2.12: Some MMI coupler examples

Self-imaging has been known and studied for a relatively long time.³⁶ However, the realization of MMI couplers have been started since the beginning of 90's.³⁸ Several analytical analysis methods of the MMI effect and couplers based on this effect are available. However, we have made use of a mode propagation

method based on effective index (2D) approximation which is explained in detail in reference⁽³⁵⁾. Using results of this method as a starting point, we designed the MMI couplers to their final version using BPM simulations. A brief summary of the method will be discussed for the sake of the completeness. The detail of our MMI couplers mask design with their BPM analysis results will be presented in Chapter 4 where the results are compared with measurements.

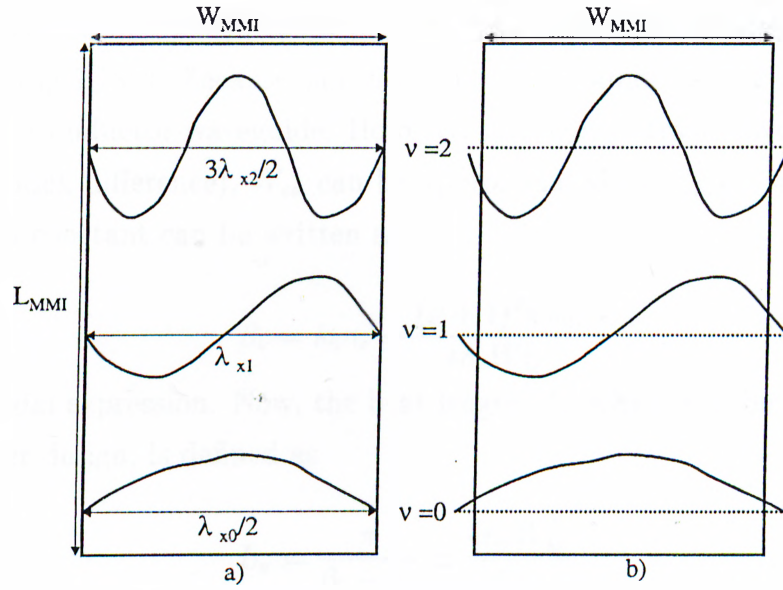


Figure 2.13: Lateral modes in a multimode waveguide with metal(a) and semiconductor(b) walls

For mode propagation analysis, modes of the multimode waveguide should be determined. For a multimode waveguide of width W_M , ridge refractive index, n_r and cladding refractive index, n_c there are m lateral modes at the wavelength λ_0 . The dispersion equation for these lateral modes can be written as

$$k_{x\nu}^2 + \beta_\nu^2 = k_0^2 n_r^2 \quad (2.35)$$

for which $k_{x\nu}$ is defined as the lateral wave number for mode ν and can be found by assuming metal MMI walls. As seen in Fig. 2.5a, metal walls require the fields to vanish at the boundaries, which result in standing waves with ν nodes for the mode ν . From the examples in Fig. 2.13a, we can write

$$\lambda_{x\nu} = \frac{2W_{MMI}}{(\nu + 1)} \quad (2.36)$$

and using the equation for wavevector (Eq. 2.7), we get $k_{x\nu}$ as

$$k_{x\nu} = \frac{(\nu + 1)\pi}{W_{MMI}} \quad (2.37)$$

and k_0 as given in Eq. 2.7. Actually, W_{MMI} should be replaced by $W_{e\nu}$ which is the effective width which takes into account the lateral penetration of each mode (see Fig.2.13b), because our multimode waveguide is not an metal one but is a semiconductor waveguide. However, for high contrast waveguides (large refractive index difference), $W_{e\nu}$ can be approximated as $W_{MMI} = W_M$. Then, propagation constant can be written as

$$\beta_\nu = k_0 n_r - \frac{(\nu + 1)^2 \pi \lambda_0}{4n_r W_M^2} \quad (2.38)$$

using binomial expression. Now, the beat length, L_π which will be important in MMI coupler design, is defined as

$$L_\pi = \frac{\pi}{\beta_0 - \beta_1} \simeq \frac{4n_r W_M^2}{3\lambda_0} \quad (2.39)$$

so the propagation constant differences are

$$\beta_0 - \beta_\nu \simeq \frac{\nu(\nu + 2)\pi}{3L_\pi} \quad (2.40)$$

An input field $\psi(x, z = 0)$ into the multimode waveguide will be decomposed into all the modes, so that

$$\psi(x, 0) = \sum_{\nu} C_{\nu} \psi_{\nu}(x) \quad (2.41)$$

If the input field is so narrow that no unguided modes are excited, $\psi(x, 0)$ can be expressed as the summation of only guided modes. The field profile at a distance z can be given as

$$\psi(x, z) = \sum_{\nu=0}^{m-1} C_{\nu} \psi_{\nu}(x) \exp[i(\omega t - \beta_{\nu} z)] \quad (2.42)$$

then writing β_0 as a common factor using Eq. 2.40 and dropping it and time dependence lead to

$$\psi(x, z) = \sum_{\nu=0}^{m-1} C_{\nu} \psi_{\nu}(x) \exp[i(\beta_0 - \beta_{\nu})z] \quad (2.43)$$

Using the Eqs. 2.40 and 2.43 the field profile at $z=L$ is

$$\psi(x, L) = \sum_{\nu=0}^{m-1} C_{\nu} \psi_{\nu}(x) \exp[i \frac{\nu(\nu+2)\pi}{3L_{\pi}} L] \quad (2.44)$$

It is possible to find some L values for which the field profile is the same as of the input field. A quick glance to the Eq. 2.44 shows that when

$$\exp[i \frac{\nu(\nu+2)\pi}{3L_{\pi}} L] = 1 \quad \text{or} \quad (-1)^{\nu} \quad (2.45)$$

the field at $z=L$ will be an image of input field. The corresponding length,

$$L = p(3L_{\pi}) \quad (2.46)$$

in which p is an integer, gives the distances for direct images of the input field for even p 's and those of mirror images for odd p 's. Similarly, the lengths at which multiple images formed can be determined to be between the direct and mirrored image lengths. The N -fold image is formed at

$$L = \frac{p}{N}(3L_{\pi}) \quad (2.47)$$

for an MMI coupler based on general interference.

The discussion made so far has not put any restrictions on excitation of the modes in the multimode section of MMI couplers and this is called *general interference*. But some different results appear when restrictions on the input come into picture. In this case, this is called *restricted interference*, which has two types: *paired* and *symmetric* interference. In paired interference case, modes numbered by 2,5,8... are not excited. This is accomplished by careful positioning of input waveguides. Only $2 \times N$ MMI couplers are possible by paired interference with N -fold image forming at

$$L = \frac{p}{N}(L_\pi) \quad (2.48)$$

where p and N should be integers with no common divisor. It is clearly understood that lengths are shortened by three times as compared by lengths of general interference. In symmetric interference case, upon which only $1 \times N$ MMI splitters can be designed, on the other hand, only even modes are excited. N -fold imaging occurs at even shorter distances which is given by

$$L = \frac{p}{N}\left(\frac{3}{4}L_\pi\right) \quad (2.49)$$

with p and N defined as integers only. $2 \times N$ and $1 \times N$ MMI couplers can also be realized upon general interference but with longer imaging distances. However, no restriction on excited modes exists for general interference, devices function with any input field (symmetric or antisymmetric) profile and any off-axis injection of input field.

2.5.1 Important Issues in Design and Characterization

There are some practical points which should be emphasized about design of MMI couplers. First of all the interference type used for the design is decided. For general interference case, input waveguides can be put anywhere and by careful adjustment the output can be optimized. There is no such a flexibility for restricted interference case. In this case the input waveguides should be symmetrically placed so that only the required modes are excited, there is not much tolerance for mistakes. It should not be forgotten that arrangement for restricted interference may lead to larger multimode waveguide widths and therefore longer MMI lengths than general interference which is the case for the 2×2 MMI couplers.

Fabrication tolerances refers to the flexibility of the device to the variations of the geometrical shape. On the other hand, *operational tolerances* is related with the variations in wavelength and shape of the input field, polarization and refractive index. The approximate relation

$$\delta L \simeq \frac{\pi n_r \omega_0^2}{4\lambda_0} \quad (2.50)$$

gives the length change which would lead approximately 0.5 dB loss.³⁷ Here the new parameter, ω_0 , is the waist of the input Gaussian beam and it can be approximated by the width of the input waveguide. The other parameters of the both fabrication and operational tolerances are related to δL through the relation³⁸

$$\frac{\delta L}{L} = 2 \frac{\delta W_M}{W_M} \simeq \frac{|\delta \lambda_0|}{\lambda_0} \simeq \frac{\delta n_r}{n_r} \quad (2.51)$$

So, high tolerance in length needs wider access waveguides, this result has led the use of the tapers at the end of the access waveguides.³⁹ Also high operational tolerances are possible if shorter MMI lengths are used.

Imaging quality, which defines how well the images are formed at the output, is another criteria for a MMI coupler design. The images should not be much wider than the access waveguides. The resolution of the MMI couplers can be estimated and it is related to the highest supported mode (m) in the multimode section. The resolution which defines minimum reachable image width, is approximately W_M/m . So the deeply etched waveguides, that is those with high rib height, will have narrower images due to their higher lateral refractive index difference which leads to confinement of larger number of modes.

Another important issue which should be considered is the possible *reflections* due to the walls of the multimode section between output waveguides. These reflections may be a problem if the MMI coupler is used for a specific application. These reflections are larger when there is high contrast and the length is not optimized. Using tapers may help in this issue.

When a MMI coupler is characterized *insertion loss*, *inter balance* and *phase* of the images are the issues to be considered. These parameters are better for an MMI coupler in general when compared with a directional coupler. Balance and phase parameters are determined by comparing any of the output image with another output image. Balancing is defined by $10 \log \frac{P_i}{P_j}$ with P_i and P_j are field

intensities of the i^{th} and j^{th} output images respectively. The unit is in dB and balancing is better when it is closer to zero.

Chapter 3

Material Properties and Device Fabrication

In this chapter, all the steps of fabrication of SOI integrated optical devices presented in this work are described in detail. Also some SOI wafer fabrication techniques are mentioned. This is needed because the techniques used in wafer fabrication directly affect the device performances.

3.1 SOI Structure and Wafer Fabrication Techniques

Silicon-on-insulator (SOI) material structure can be defined as a relatively thin silicon ($n \sim 3.5$) top layer separated from a thicker silicon substrate by a thin insulator which is SiO_2 ($n \sim 1.45$) in general, as seen in Fig.3.1.

SOI does not mean that the insulator is always SiO_2 . There has been another SOI material which is known as silicon-on-sapphire (SOS). The idea to separate a silicon layer from the substrate has started with SOS since 1960's. SOS is not so good due to its poor material properties, high defect density in silicon films and the high dielectric constant of sapphire limiting device performances.

The point is to make use of the SOI structure while having the active silicon

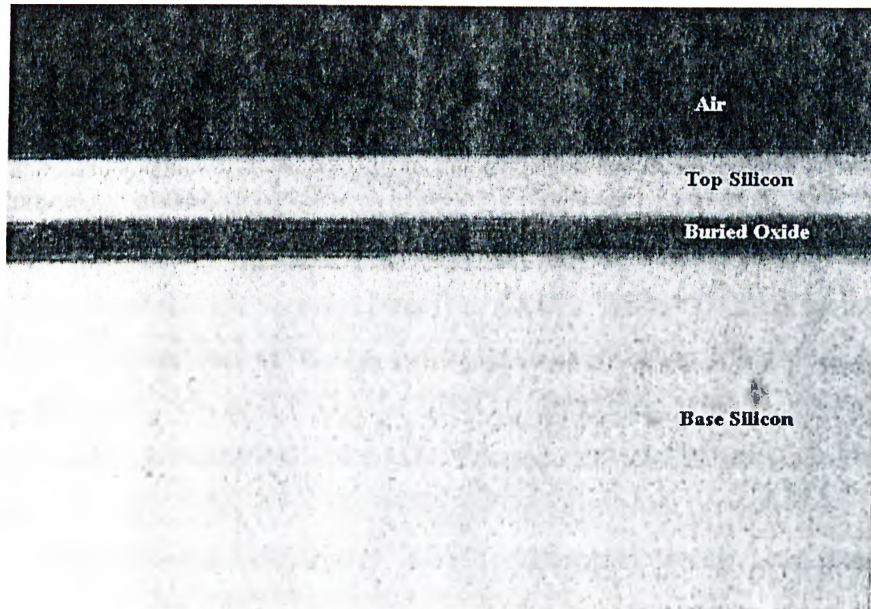


Figure 3.1: A picture of SOI structure

fabricated with the same quality as bulk silicon. The criteria needed to be better in SOI fabrication are defect density, layer interface and silicon surface roughness and thickness uniformity. These have been the categories in which different SOI material fabrication techniques compete. Since the use of SiO_2 as an insulator was started, several techniques have been developed and utilized for realization of SOI material most of which have remained only as a research interest. Among these, growing single-crystal silicon films on SiO_2 using lateral epitaxy by seeded solidification⁴⁰ deserves to be cited. However, it does produce SOI material with properties even worse than SOS. The winners of the competition, Separation by Implimented Oxygen (SIMOX) and Bond and Etch-back (BESOI) technologies have emerged after 1980's. They are the only technologies which succeeded in being commercial products and have started to be used in both SOI based integrated electronics and integrated optics.

Separation by Implanted Oxygen (SIMOX) Technology

The simple layout of SIMOX process is as follows; an oxygen ions (O^+) beam of doses as high as $1 - 2 \times 10^{18}$ ions cm^{-2} is accelerated to penetrate into a silicon wafer surface by about $0.1-0.2 \mu m$ under a electrical potential of $150 - 200 keV$ to produce a SiO_x insulating layer with $0.1 - 0.5 \mu m$ thickness.⁴¹ This is then followed by a high temperature anneal at $1250 - 1300 ^\circ C$. This annealing step facilitates the crystallization of the damaged thin top silicon layer and formation of a relatively sharp Si and SiO_2 . In SIMOX technology different Si thicknesses become available by implantation at different O^+ doses and under different potentials. In any case, the layer thickness obtained by SIMOX is limited. Whereas, the thickness uniformity is well controlled which is of the order of $\pm 5\%$.

Bond and Etch-Back (BESOI) Technology

All the different techniques under the name, BESOI, have the same starting procedures. One of the two silicon wafers used is oxidized by either wet or dry oxidation techniques (e.g. thermally grown SiO_2) while the other wafer is hydrophilically bonded with the oxidized wafer (The oxide layer then functions as the buried insulator). Then, what makes difference among different BESOI techniques is the way they use for thinning one of the silicon wafers to get the silicon film with desired thickness. The simplest way of handling this thinning task is to polish the wafer until the desired thickness, which can be as small as $1 \mu m$ or as large as a few hundred microns, is reached.⁸ Also some etching mechanisms enhanced by some etch stop layers are also being utilized.^{8,42} However, the uniformity of the silicon film thickness may become a problem with these techniques due to lack of sensitivity of polishing and etching mechanisms.

There have been a clever solution to this problem, *the smart-cut* technology. In this process,⁴² the wafer which will be oxidized is previously implanted by hydrogen ions of doses $2 \times 10^{16} - 1 \times 10^{17}$ ions cm^{-2} . Then two wafers are bonded as described before, and followed by a two step heat treatment at temperatures of

400 – 600 °C instead of direct polishing or etching as in the previous techniques. This leads the hydrogen ions implanted wafer to split into one thin silicon layer bonded to the other wafer with SiO₂ between them and a thick silicon layer which can be used in another process as the bottom wafer. The final step in all techniques is the fine polishing of the top silicon layer. The general BESOI and smart-cut procedure layout are schematically described in Fig.3.2. The basic advantage of smart-cut is that the thickness uniformity as good as those achieved in SIMOX technology is possible.

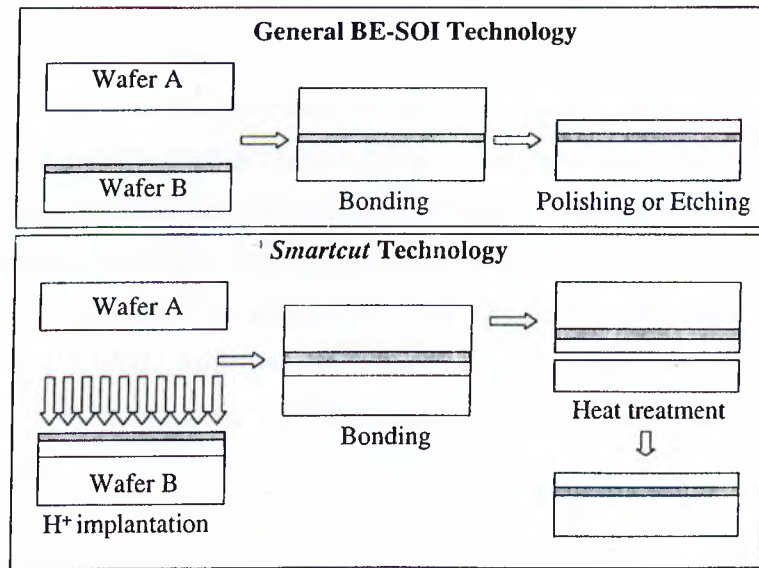


Figure 3.2: Process layout of BESOI and *smart – cut* technologies

When SIMOX and BESOI are compared, it can be said that SIMOX provides good SOI structures for both digital and analog integrated electronic circuit applications and is not preferred for integrated optics systems in general . Whereas, BESOI wafers are better SOI platforms for integrated optic devices and systems with providing defect densities as low as bulk silicon and various silicon layer thickness options. We used BESOI wafers with various silicon thicknesses in integrated optical devices presented in this work.

3.2 Sample Preparation

Preparation of SOI samples for further fabrication processes, photolithography and anisotropic chemical wet etching (in *KOH* solution), includes cleaving of pieces from a whole SOI wafer of 100 or 125 or 150 *mm* radius, cleaning and finally masking material (*silicon nitride*) deposition of the samples. The whole fabrication process including sample preparation is done in the class 100 facility available at Bilkent University Advanced Research Laboratory. The pieces cleaved out from SOI wafers have sizes depending on the mask used to translate waveguides, directional couplers and MMI couplers patterns to samples. Typical sample sizes are 12x18 *mm* for straight waveguides, 12x10 *mm* for directional couplers and 10x15 or 12x20 *mm* for MMI couplers. A wafer is drawn by a diamond point pencil to define the samples, which must have edges perpendicular or parallel to the principal axis of the wafer, then the wafer is sandwiched between two glass plates so that the drawn line be on the edges of two glass. After that an direct and instant force is applied on the wafer part remained outside of the sandwich with a metal, rounded tip stick, this leads the wafer cleave into two parts through the drawn line. Further cleavage is applied if necessary to define smaller samples.

3.2.1 Sample Cleaning

The cleaved samples are first blown with nitrogen to remove any tiny crystal pieces remaining on them. Then, they are cleaned through the process called *tri - solvent* cleaning. These solvents, trichloroethane (TCE), acetone (ACE) and iso-propanol (ISO) are put in different clean, glassware containers. Samples are first put in TCE solvent boiling on a hot plate for 3 minutes. Then they are directly put in ACE at room temperature and left there for 5 minutes and finally put into ISO solvent also boiling for another 3 minutes. The tri-solvent cleaning of samples is finished by exposing them to flowing deionized water (DI). Through this process samples are carried in a rinser. Tri-solvent cleaned samples are one more time blown with nitrogen while lying on a tissue paper to remove the

remaining water droplets. Before finishing the cleaning process, the cleanliness of each sample is controlled under optical microscope. If any of them is not clean enough, they are put into a ACE bath at room temperature and their surfaces are scrubbed with a ACE soaked q-tip. This is an effective way for removing any remaining dirt after tri-solvent cleaning. If the samples are verified as clean they are put on a hot plate at 110 °C for 1 minute in order to evaporate remaining monolayer of water on the sample surface.

3.2.2 Masking Material Deposition

The realization of integrated optic devices on SOI samples is achieved by etching some parts while preserving the others. For waveguides, the straight strips should be preserved in the etching process. KOH solution which is an selective etchant for crystal silicon is used in our fabrication process, and will be explained with all the other etching details later in this chapter. We make use of a thin layer of silicon nitride (Si_3N_4) film, which shows very high resistance to KOH solution, as a mask. SiO_2 have also been widely used as masking material in the same purpose. Apart from their resistance to the KOH solution, their simple processing through hydro fluoric acid (HF) makes them the primary choices for masking material to be used in KOH based etching processes.

Si_3N_4 films are deposited using the standard plasma enhanced chemical vapor deposition (PECVD). PECVD is an extended version of chemical vapor deposition (CVD) in which the reactants are brought to the vicinity of the hot sample by gas flow and appropriate chemical reactions take place to grow the material of interest on the sample surface. Normal CVD reactions require the samples to be at temperatures as high as 700 to 1000 °C.⁴³ PECVD makes use of plasma reactions to assist the CVD reactions taking place which result in the samples being deposited at relatively low temperatures(100 – 350 °C).

PECVD process is conducted in *plasma reactors* which may be in barrel (or tube) or planar or downstream configurations. A fully automated planar plasma reactor (see Fig.3.3) have been used for Si_3N_4 deposition in our fabrication process

(Plasmalab 8510C).

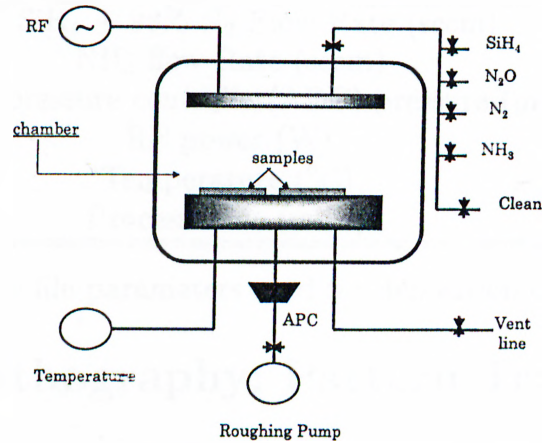
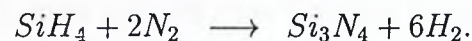


Figure 3.3: PECVD reactor structure

Cleaned samples are placed on the lower electrode plate which is heated before the process starts. The plasma is created via excitation by 13.56 *MHz* radio frequency (RF) which is applied across the electrode plates. The gases used in the process come into the reactor from the specific valves placed at its walls. In general, PECVD grown films have characteristics (refractive index, film thickness etc.) which depend on the following reactor and process parameters; gas type, gas flow rate, RF power, sample temperature and sample material.

In Si_3N_4 deposition, we make use of 2 % silane (SiH_4) diluted in 98 % nitrogen (N_2) as the silicon source and ammonia (NH_3) as the nitrogen source. Two possible chemical reactions taking place during plasma process are



We are not interested in material characteristics of the deposited Si_3N_4 except its thickness, since it is not included in final product and to be removed after the realization of the waveguides with *KOH* etching. The recipe file which result in 2000 Å thick Si_3N_4 film when applied is given in Table 3.1.

2% SiH ₄ + 98% N ₂ Flow Rate (sccm)	180.0
NH ₃ flow Rate (sccm)	45.0
Automatic pressure controller(ADC) pressure (mTorr)	1000.0
RF power (W)	10.0
Temperature (°C)	250.0
Process time (mins)	20.0

Table 3.1: The recipe file parameters used for deposition of Si₃N₄, masking film.

3.3 Photolithography; Pattern Transfer

After masking material is deposited, it is the turn of the step, to transfer the pattern from a mask to the sample. Masks have clear and opaque parts defining the patterns. In our waveguide mask, the waveguide strips are defined as opaque while their surroundings is clear. This pattern transfer to a sample surface from a mask is done by lithography methods. In this process, samples are first applied with photoresists (PR), then the mask is carefully positioned on the alignment tool to align sample and the mask and the sample is exposed with UV light and this process is called *photolithography*. After exposure, the samples are treated with a special solvent called *developer*. This solvent dissolves the PR parts which are exposed, that is parts remained under the clear part of the mask during exposure, if the PR is *positive*.⁴⁴

In our case, the exact photolithography process can be explained in detail as follows. The samples are put on the spinning chuck of the spinner tool(Karl Suss Model SM 120 Spinner) and a drop of 100 % HexaMethylDisilazene (HMDS) solution is put on the sample surface to enhance the adhesion of the PR to the sample and the sample is spun at 5000 *rpm* for 40 *s* so that HMDS is uniformly spread over the sample surface. The PR we use is a positive PR and has the label, AZ5214E. After covering all the sample surface with the PR drops, the sample is ones more spun at the same rate for 40 *s*. The uniformly PR covered samples are prebaked on a hot plate at 120 °C for 50 seconds to strengthen the sticking of PR to the sample and eliminate the stickiness of the PR. The resulting

PR film has a thickness of $1.6 \mu\text{m}$ which is measured after photolithography and developing steps with Sloan Dektak 3030ST Surface Texture Analysis System. The mechanisms we used for both mask alignment and exposure are integrated under the label of Karl-Suss MJB-3 HP/200W Mask Aligner. This is a system that uses a 500 W mercury xenon high pressure lamp as its light source and in principle can define dimensions as small as $0.8 \mu\text{m}$ with $0.1 \mu\text{m}$ accuracy. The mask is loaded on the mask holder of the aligner and the sample and patterns on the mask are aligned such that the waveguide strips or the straight sections of the other devices are parallel or perpendicular to the edges of the rectangularly cleaved sample. The SOI samples used have surfaces on $\langle 100 \rangle$ plane and the strips are defined on that plane also. This choice of alignment lets us make use of the anisotropic characteristic of KOH etching which will be discussed in next section. After exposure, the exposed PR parts are dissolved in 25 % aqueous AZ400K developer solution and this results in realization of the mask patterns in the PR film. The structure is in the form of PR strips on Si_3N_4 film which is on SOI substrate.

The sample is still not ready for KOH etching. These PR strips must be transferred into Si_3N_4 strips, the actual mask for KOH etching. For this purpose the Si_3N_4 between PR strips should be removed and this can be done by etching Si_3N_4 in diluted HF solution. In this etching step, the masking material becomes PR. Before this etching process, the PR stripes or patterns are further hardened via another baking process with same temperature and duration as the prebake. This baking is called the postbake. The HF solution has ratio 1 : 30 for $\text{HF}(50\%) : \text{H}_2\text{O}$ and etches all of the 2000 \AA Si_3N_4 in 15 seconds. The new structure is PR strips on Si_3N_4 strips over SOI substrate. The PR strips are then removed by acetone (ACE), since they are not needed anymore. Finally our samples with Si_3N_4 patterns on them are ready for final etching in a KOH solution.

3.4 Anisotropic KOH etching

Waveguides must be defined on the top layer of the SOI samples. *Dry* and *wet etching* techniques can be employed for this purpose. In both techniques, the unmasked silicon between Si_3N_4 strips on SOI samples are removed. Dry etching uses physically assisted chemical radicals and ions, which are produced in a plasma reactor, to etch the semiconductor material surface, both chemical. Dry etching which can be called as *reactive ion etching* (RIE), results in an anisotropic etching profile. That is, some special planes of semiconductor crystals are preferably etched at a higher rate than other planes. On the other hand, wet etching being the most widely used etching technique makes use of chemical reactions taking place between semiconductor material and aqueous acidic and basic solutions. Unlike dry etching, wet etching is generally isotropic for the most semiconductor material and etching solution pair, but also some examples of anisotropic wet etchants exist.

Both dry etching (or RIE)^{8,25-27} and wet etching^{18,28} have been applied in silicon-on-insulator based waveguide device fabrication. During the initial stages of this research, we had to decide on the etching technique to be applied. Using some criteria which are stated below, we decided to make use of aqueous potassium hydroxide (KOH) solution which is one of the anisotropic wet etchants of silicon. The points considered were as follows. (1) If possible, the etching technique to be used should be simple and easy to apply. Wet etching techniques do not require complex equipment and are simple in general, unlike RIE process. (2) The anisotropic etching techniques would be preferred to the isotropic ones in our case, since, isotropic etching causes the waveguides be narrower than the strips on the masks, an effect called *undercut*, and the available strips on the mask are limited with widths 2, 3, 4, and 5 μm which are not suitable for the process leads undercut. KOH is a natural and good choice under these conditions because it has been used widely in silicon micromachining technology and is easy to apply and does not need any complex equipment. Also, waveguide profiles without undercut are possible with KOH etching as described in Fig. 3.4.

KOH anisotropic etching of silicon have been studied a lot since the early 60's.^{45,46} The etch characteristics studied are the etch rates for different KOH concentrations and etch temperatures for various silicon crystal planes with and without stirring the solution. The type of the silicon surface((100) or (110))and the orientation of the mask strips on the sample determine the waveguide profile. The Fig.3.4 shows the resulting crosssectional waveguide profiles on a (100) silicon surface.

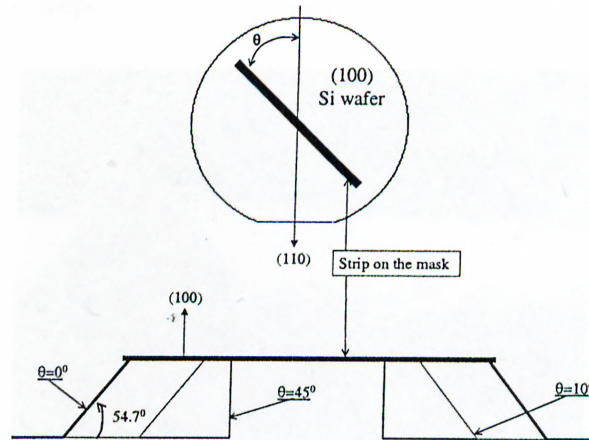


Figure 3.4: Effect of the waveguide strip orientation on the waveguide profiles on (100) surface

When starting, we knew very little about anisotropic KOH etching. We could only start with some parameter values from KOH etching literature but the process had to be optimized for the best result. The goals for KOH etching process optimization were to realize waveguides with no or very small undercut, get smooth waveguide walls and smooth inter waveguide surfaces. This is the key point for low loss waveguides. Finally, we need to find a reasonable etch rate. These goals are reached one by one and changing only one parameter while keeping the others unchanged. The parameter to be controlled was solution concentration, etch temperature, stirring and HF dip application before starting etching.

For optimization process silicon samples instead of SOI were used , since SOI wafers are more expensive. The samples were prepared for the etch trials through

the procedures explained in previous sections. The waveguides are patterned on the (100) silicon samples so that they are either parallel or perpendicular to the primary axis of a (100) silicon wafer. In other words, θ was chosen as 0 (see Fig.3.4). This choice ensured that the waveguides will be fabricated with minimum undercut. Good waveguide profiles but very rough sample surfaces were seen after first trials (see Fig.3.5 and 3.6). The top layer in the pictures is the Si_3N_4 and the undercut seen is probably due to missalignment of the mask in photolithography step.

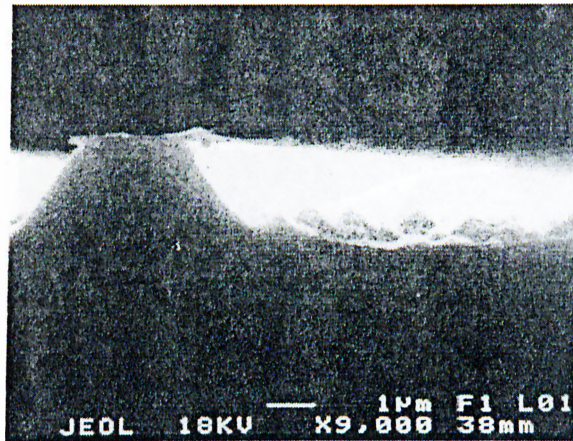


Figure 3.5: SEM photograph of the initial etching results; waveguide profile

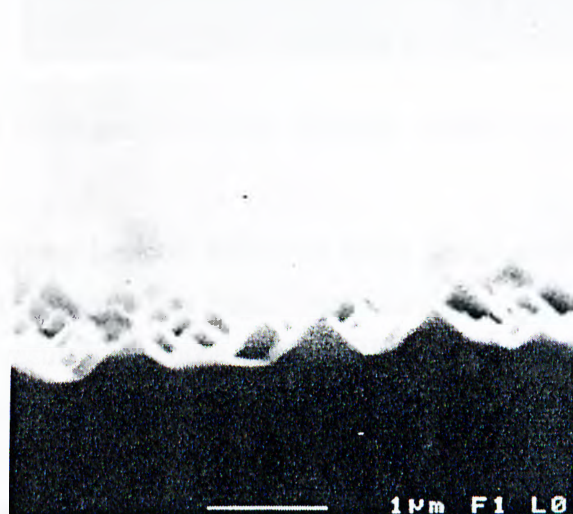


Figure 3.6: SEM photograph of the initial etching results; surface

In first etching trials KOH:H₂O ratios of 1:4, 1:10 and 1:20 were employed at temperatures of 80, 70, 55 and 50 °C. The solution was put on a hot plate which uses a probe placed in the solution to control and fix the solution temperature at the set value. The hot plate also has stirring capability. All initial trials resulted in rough surfaces for example, the waveguide seen in Fig.3.5 was etched with 1:20 KOH:H₂O solution at 50 °C. Numerous etch trials with KOH dissolved in H₂O resulted in high etch rates but rough surfaces.

To smoothen the surface we tried adding some iso-propanol(ISO) as a wetting agent. A solution KOH:H₂O:ISO with 1:3:1 ratio was used for etching at different temperatures, 85, 40, 35, 30 °C with no stirring. Almost perfect smooth surfaces and rib walls were obtained at 40 °C with this solution (see Fig.3.7).

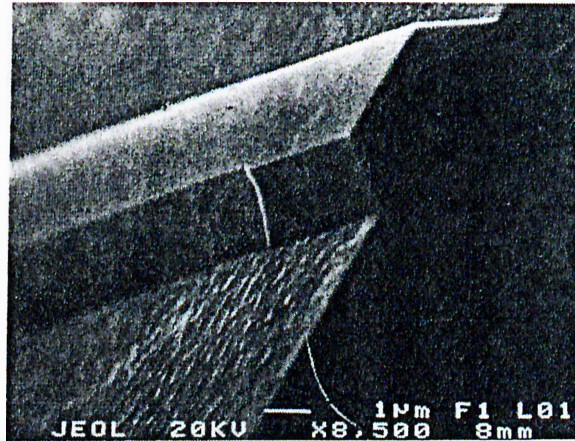


Figure 3.7: SEM photograph of the etching results at 40 °C ; surface and waveguide walls

The surface smoothness became better at lower temperatures but periodic hills started to build on rib walls (see Fig.3.8 and 3.9).

In lieu of these results, we chose 1:3:1, KOH:H₂O:ISO solution at 40 °C as our optimum parameters. Samples were treated with diluted HF(1:100) for 2 seconds to etch away native silicon-oxides on SOI surfaces. This recipe have been used for anisotropic etch of SOI waveguides, directional coupler and MMI couplers (see Figs.3.10, 3.11 and 3.12). The etch rate for this recipe is not constant with time which is a general property of anisotropic KOH etching, but, the etch rate

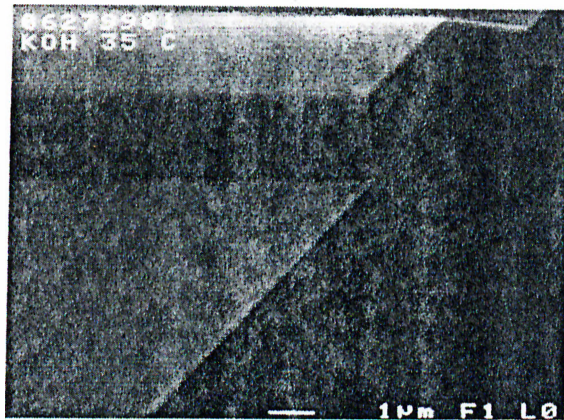


Figure 3.8: The etching results at 35 °C; surface and waveguide walls.



Figure 3.9: The etching results at 30 °C; surface and waveguide walls.

remained in the range of 550 to 650 Å/min for 0-35 minutes long etch process during which etch depths upto 2.2 μm were reached. The other parameters that may affect especially the repeatability are the total volume of the solution and the stability of solution temperature. Larger solution volumes and more stable solution temperature result in better etch results.

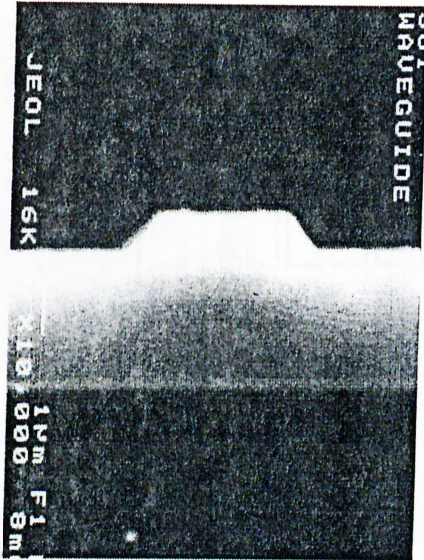


Figure 3.10: SEM photograph of a cross section of a SOI waveguide fabricated by KOH etching.

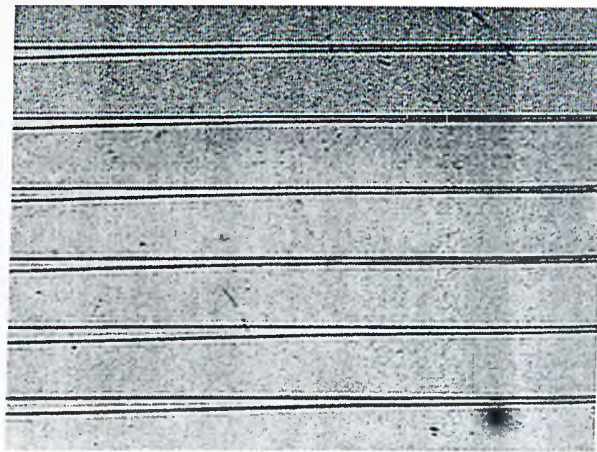


Figure 3.11: A top view photograph of SOI directional couplers fabricated by KOH etching; the lines closer to each other are straight waveguide sections.

Backside Thinning

After fabrication of waveguides, samples have to be prepared for optical measurement. That is, samples are cleaved in order to get waveguide facets

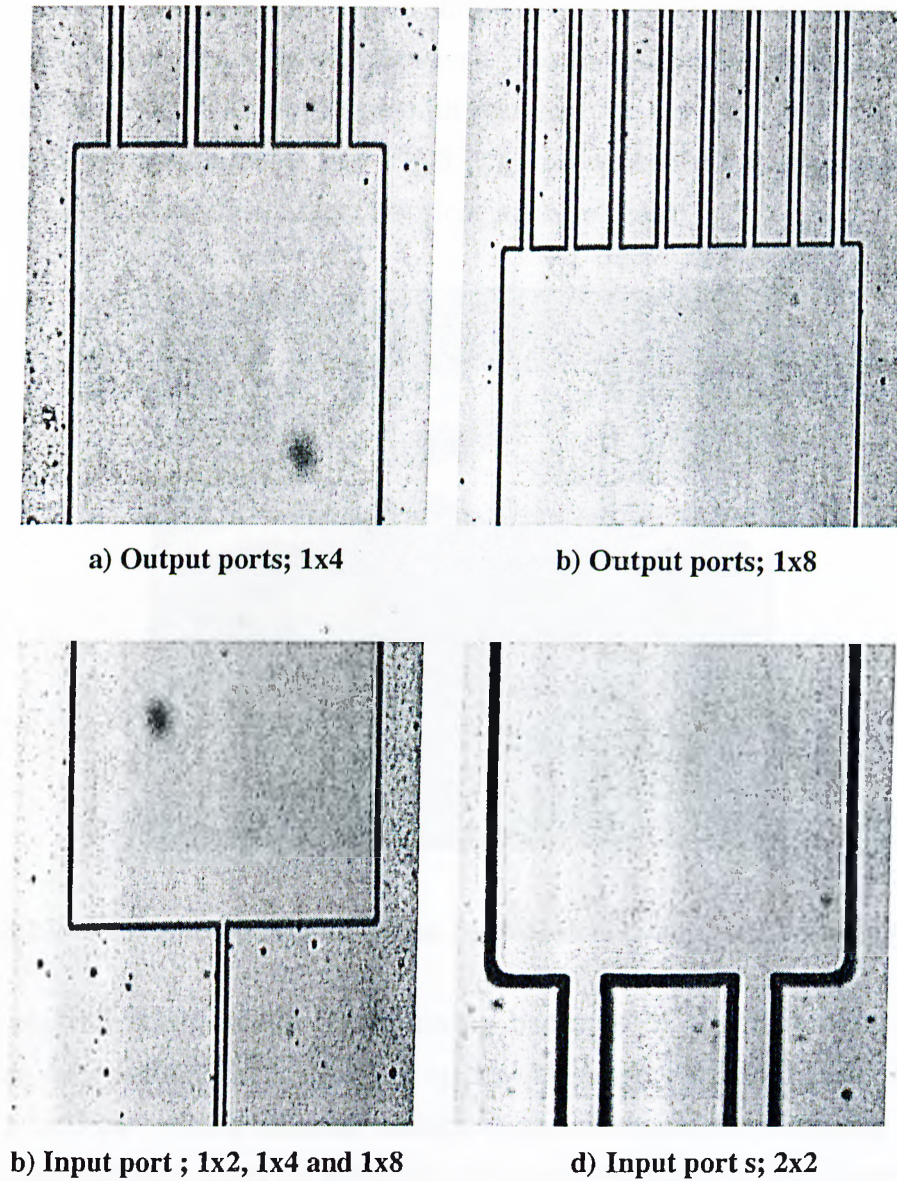


Figure 3.12: Top view photographs of input and output ports of SOI MMI couplers fabricated by KOH etching.

with optical quality. This cleavage process is different from the process used to cleave a whole wafer into small samples. This so-called *optical quality cleavage*

process is accomplished by first open a small trench at one edge of the sample then rounding a metal stick with rounded shape tip on that trench to make sample be cleaved through a crystal layer. However, due to the buried oxide layer, optical quality cleavage of SOI samples was an problem for us. Our first trials resulted in very bad waveguide facets (see Fig.3.13), and we could not even see the mode profile of these waveguides during optical measurement.



Figure 3.13: SEM photograph of a bad (not optically cleaved) waveguide facet.

We resolved this problem by thinning backside of the SOI samples after waveguide fabrication, then applying optical cleavage. KOH etching was used one more time but with a different etching recipe. In *backside thinning* process, two SOI samples were stuck to two sides of a dummy silicon crystal piece with a black-wax on a hot plate at 120 °C. During sticking, processed surfaces (devices fabricated on them) of the two SOI samples were applied with black-wax and backsides remained clean. This stack of crystal pieces are put into a previously prepared KOH solution (KOH:H₂O ratio was 1:3) stabilized at 50 °C over which black-wax starts to melt. During the thinning the solution was stirred at 150 *rpm*. The approximate etch rate was 13.6 $\mu\text{m/hr}$ and samples were thinned to

100-125 μm with that rate. After thinning is over the samples are removed from the silicon piece on the hot plate and cleaned from black-wax with TCE. Samples were then optically cleaved, the results were encouraging (see Fig.3.14), that is, some of the facets were good enough for optical measurements but some were still bad.

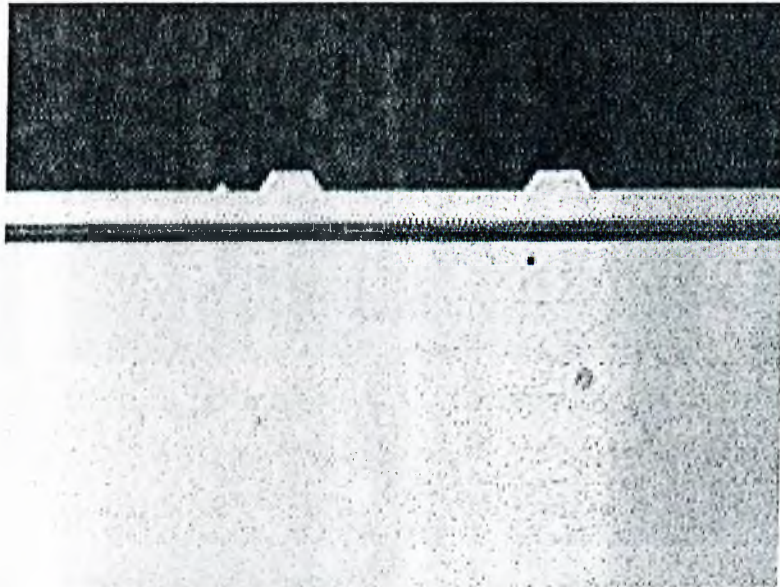


Figure 3.14: Photograph of optically cleaved waveguide facets.

A summary of all the fabrication steps can be seen in Fig.3.15.

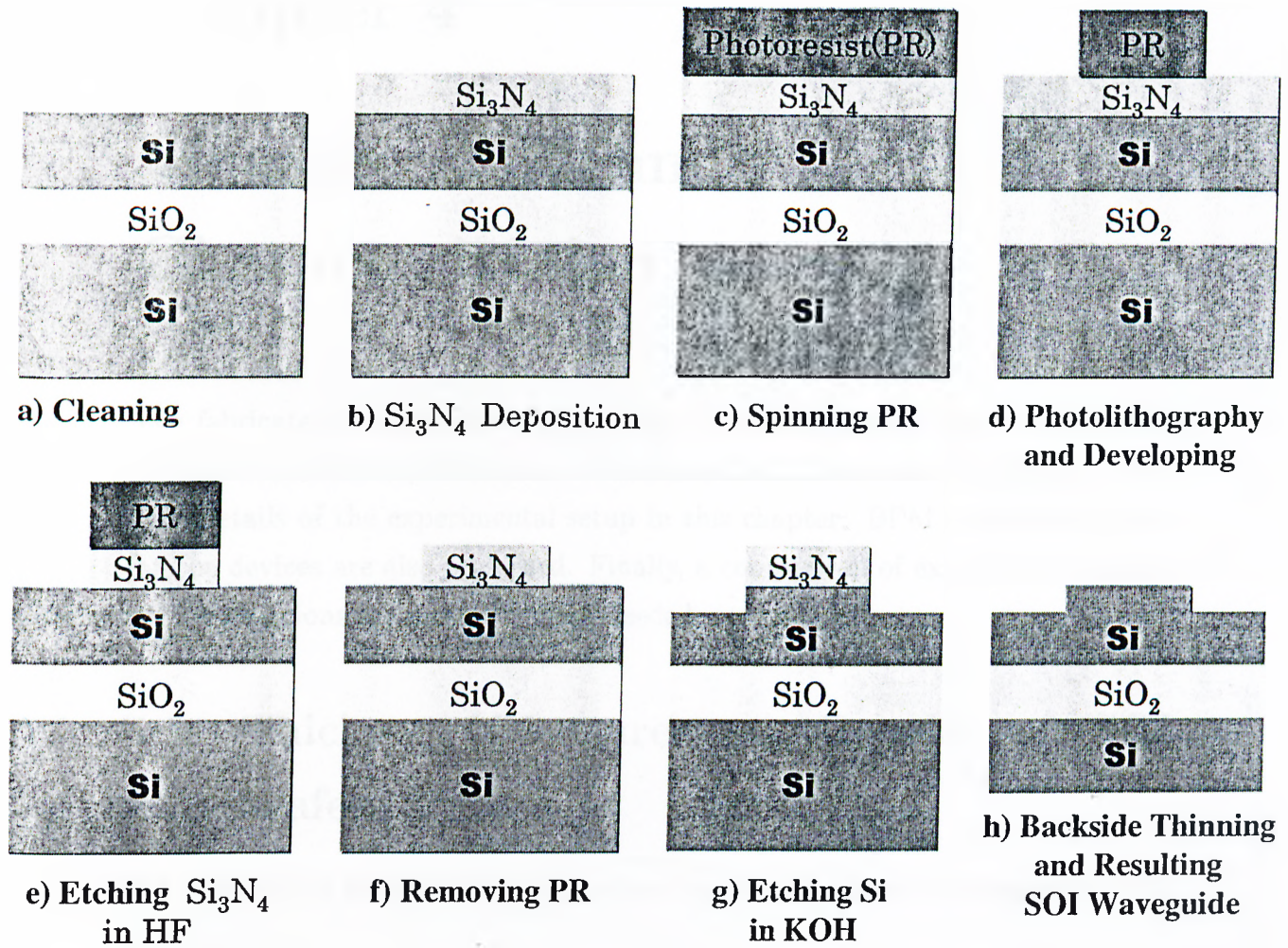


Figure 3.15: All steps in fabrication of SOI optical waveguides.

Chapter 4

Measurements and Characterization

The fabricated SOI integrated optical devices were characterized using standard optical measurement techniques. All the results of the measurements are given with details of the experimental setup in this chapter. BPM simulation results for the devices are also presented. Finally, a comparison of experimental results with simulations are provided when needed.

4.1 Thickness Measurement Results of SOI Wafers Used

SOI wafers used in device fabrication were purchased with the thicknesses given in Table 4.1

#	Top Si Layer (μm)	Buried SiO ₂ Layer (μm)	Base Si Layer (μm)
Wafer 1	3	1	630
Wafer 2	4	1	424
Wafer 3	5	1	525

Table 4.1: The thicknesses of SOI wafers used.

For SOI waveguide devices analysis, fabrication and characterization, the correct knowledge of silicon top layer and buried oxide layer thicknesses is necessary. Therefore, relevant thicknesses were measured to verify the specifications of the purchased SOI wafers.

The thickness measurement was performed as follows; tiny slices were cleaved from each of the wafers radially as seen in Fig. 4.1. These long slices were then cleaved into smaller crystal pieces. Pictures of the layers were taken using scanning electron microscope (SEM, Model JEOL-JSM 6400) for each piece of crystal. Two cross sectional SEM pictures of Wafer 2 are given in Fig.4.2 where the radial distance, d was measured from the edge of the wafer. As seen in Fig.4.2, silicon top layer does not start from the edge of the SOI wafer. The measured thicknesses are plotted in Figs.4.3 and 4.4 as a function of the distance to the wafer edge (d).

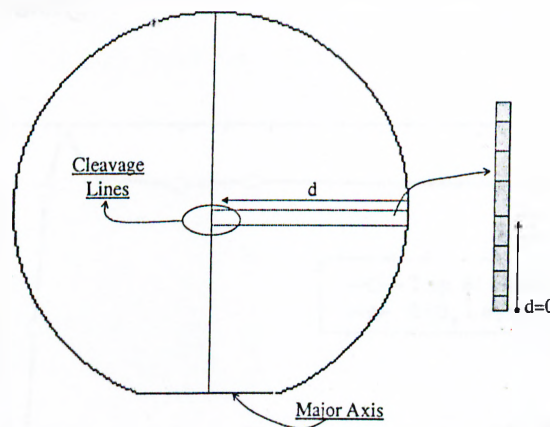


Figure 4.1: A slice taken from a wafer for layer thickness measurement.

These measurement results show us that layer thicknesses are consistent with the values given in Table. 4.1 within the error limits which are typical for BESOI wafers. As for the oxide thicknesses, the BPM simulation results for different thicknesses show that thicknesses above $0.1 \mu\text{m}$ are enough to prevent optical power leakage to base silicon layer (see Fig.4.5). Buried oxide layers of the SOI wafers used, which are measured to be approximately $1 \mu\text{m}$, ensure that we are well apart from cutoff oxide thickness. Therefore, the assumption of SiO_2 as

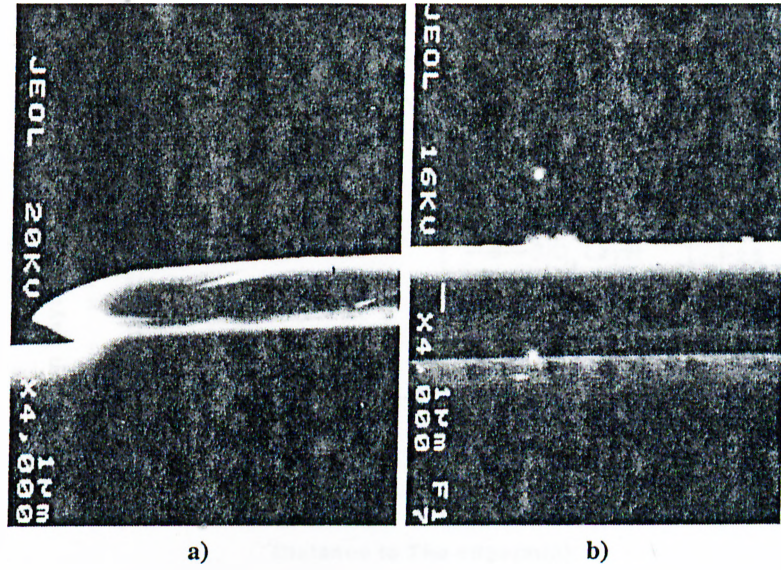


Figure 4.2: SEM photographs of layers taken at (a) 0.8 mm and (b) 39 mm to the wafer edge for Wafer 2.

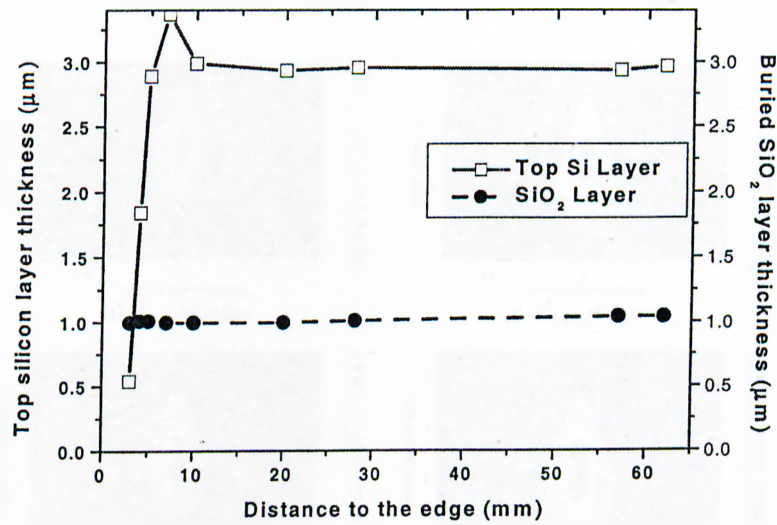


Figure 4.3: Measured layer thicknesses for Wafer 1.

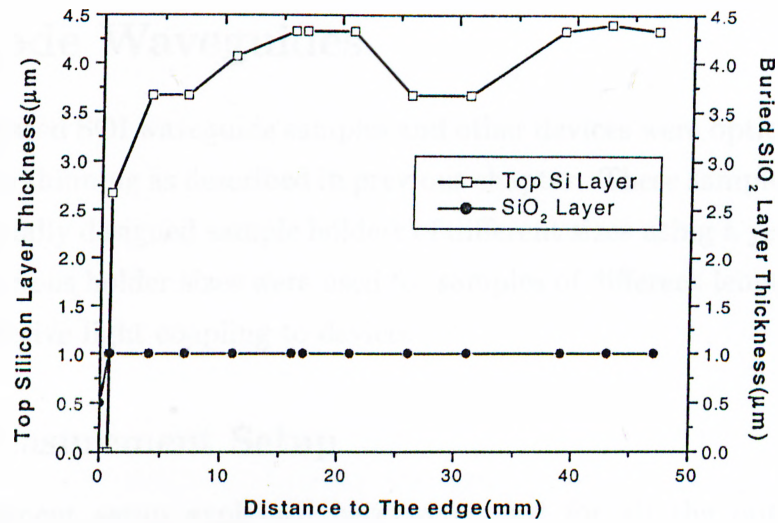


Figure 4.4: Measured layer thicknesses for Wafer 2.

the substrate and silicon top layer thicknesses as waveguide height in design and BPM simulation of SOI integrated optical devices are reasonable .

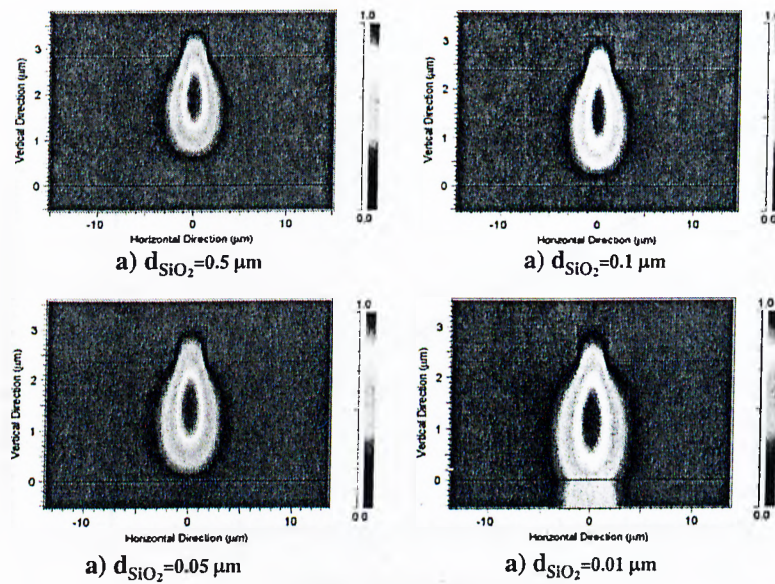


Figure 4.5: BPM simulations of optical power confinement for a SOI rib waveguide of different SiO₂ layer thicknesses.

4.2 Characterization of SOI Optical Single Mode Waveguides

All the fabricated SOI waveguide samples and other devices were optically cleaved after backside thinning as described in previous chapter. These samples were then glued on specially designed sample holders of different sizes using a yellow crystal wax. Here various holder sizes were used for samples of different lengths and this enhances effective light coupling to devices.

4.2.1 Measurement Setup

The measurement setup explained here were used for all the optical device measurements. The setup uses a *DFB* (Distributed FeedBack) laser as its IR light source. This laser lases around 1550 nm but the peak value could move by a few nm by changing the laser temperature. Optical measurements were generally performed with the laser being at 25 °C and under 27 mA current. The laser has a peak value of 1547.58 nm under this condition (see Fig.4.6).

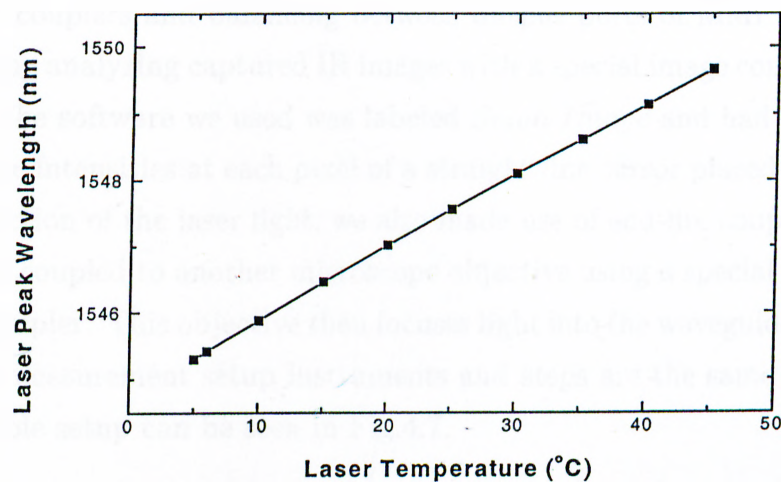


Figure 4.6: DFB laser wavelength peak value variation with laser temperature.

Fiber-laser integration enables light to be transferred to a single mode (SM) fiber with core size of $9\ \mu\text{m}$. This SM fiber is attached to another SM fiber which is bent to form a number of circles with diameter of a few cm and placed in three circular mounts. This specially designed SM fiber is called *polarization controller* and enables us to measure device performances at both TE and TM polarizations. It controls polarization while moving the mounts from transverse to longitudinal state or vice versa. The polarization controller is attached to a third SM fiber whose optically cleaved end is positioned in a fiber-chuck on a XYZ translational stage. In butt coupling case, light is directly coupled into waveguides through the cleaved fiber end. Sample holders can also be moved on another XYZ translational stage to enhance the fiber-chip coupling. Light coming out of the waveguides end facets is collected and then focused to either an Ge photo detector or an IR camera using a microscope objective. The detector measures output optical power when attached to an oscilloscope or optical powermeter. Optical power measurements are then used for calculating optical losses. IR camera was used for careful positioning of optical modes before power measurement and visualization of modes. A number of neutral density filters were used to control optical power to avoid saturation of the camera when the images captured to image files using a video capture card attached to a PC. Coupling properties of directional couplers and balancing between output ports of MMI couplers were calculated by analyzing captured IR images with a special image contrast analysis software. The software we used was labeled *Scion Image* and had the ability to read relative intensities at each pixel of a straight line cursor placed on an image.

For injection of the laser light, we also made use of end-fire coupling in which case light is coupled to another microscope objective using a special optical fiber-objective coupler. This objective then focuses light into the waveguide facets. The rest of the measurement setup instruments and steps are the same as explained and the whole setup can be seen in Fig.4.7.

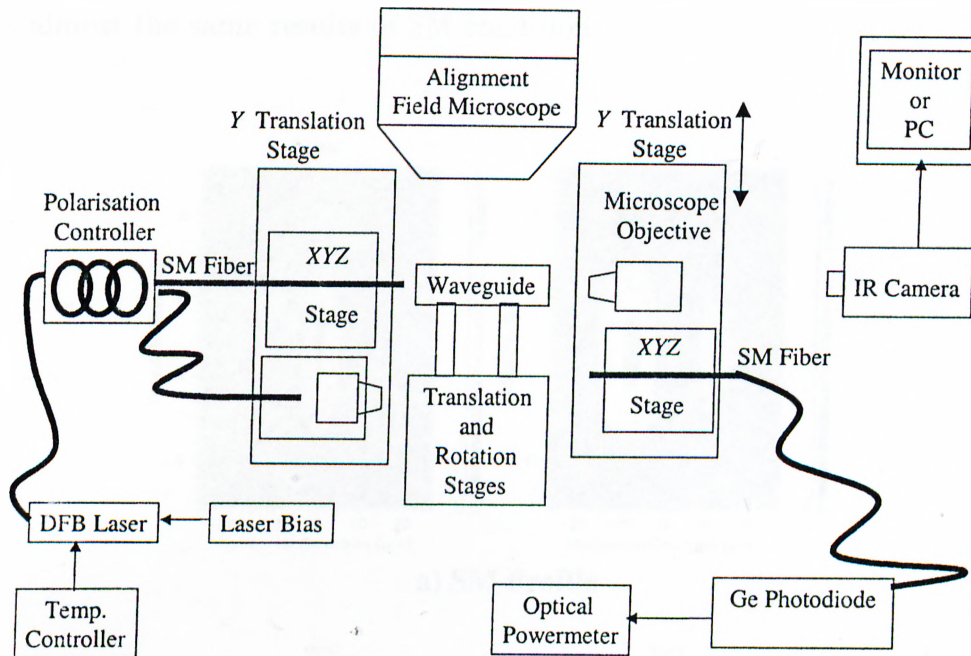


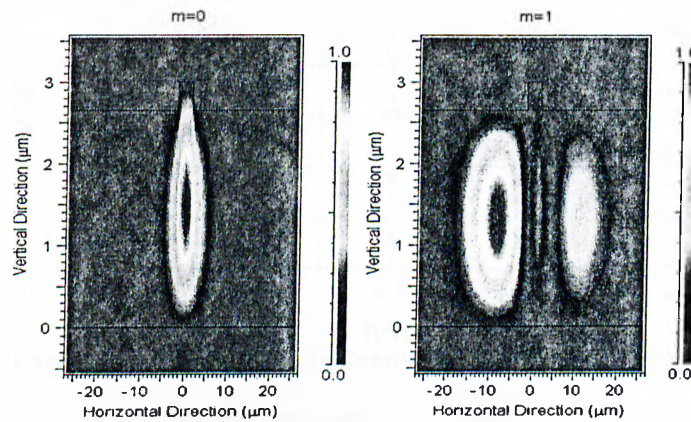
Figure 4.7: Optical measurement setup.

4.2.2 Verification of Single Mode Condition

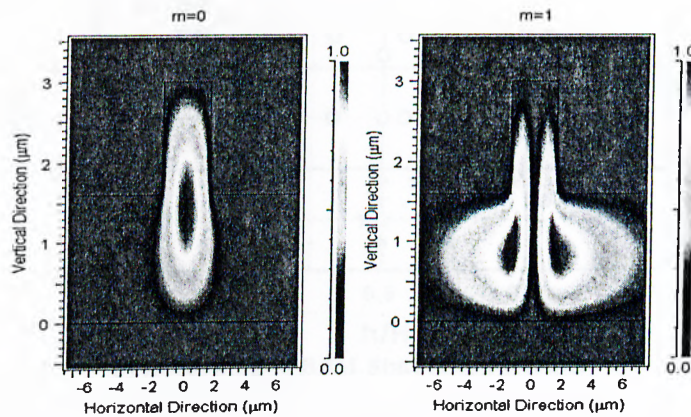
The single mode (SM) condition explained in Chapter 2 (Eqs. 2.20 and 2.21) is based on EIM analysis. However, the real SOI rib waveguide has a 3-D structure. For that reason the validity of SM condition in 3-D SM rib waveguide design has to be verified. We evaluate SM condition using two different ways, BPM simulation results and experimental results.

First a number of SOI rib waveguide structures with different waveguide parameters (width, w , height, H and slab height, h) were chosen. Some of these structures correspond to multimode (MM) waveguides while the others to SM ones, according to SM condition. BPM was then used to simulate some of these structures. In BPM simulations transverse mode profiles of these waveguides were computed. These profiles were then analyzed to determine those which were SM or MM. Some transverse mode profiles computed during these BPM

simulation runs are given in Fig.4.8. As can be seen in Fig.4.9, BPM simulations gives almost the same results of SM condition.



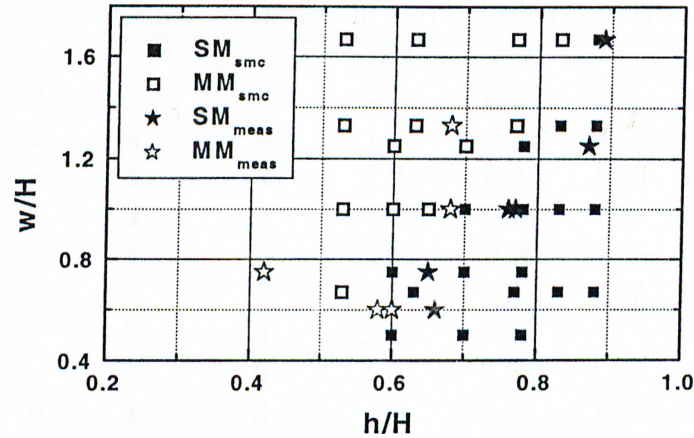
a) SM Profile



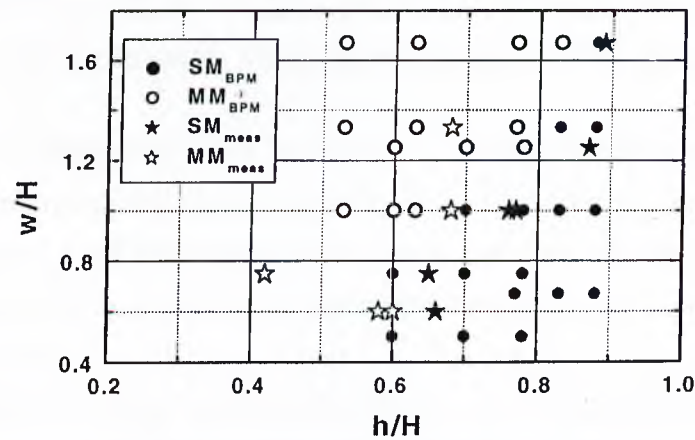
b) MM Profile

Figure 4.8: Transverse fundamental and first excited mode profiles of a SOI SM (a) and MM (b) waveguide structure computed using BPM.

Then, a number of SOI rib waveguides with different w/H and h/H ratios were fabricated and their modal properties were analyzed on the optical measurement setup. The geometrical dimensions of SOI straight waveguides analyzed are given in Table 4.2 with results of modal analysis. The results



a) According to Single Mode Condition for Rib Waveguides



b) According to BPM Simulation Results

Figure 4.9: Comparison of BPM simulation results (b) with SM condition results(a).

are also displayed in Fig.4.9 in order to compare with the other evaluation means. Experimental results shows a behaviour totally fitting to the single mode condition and BPM simulations.

During analysis of waveguides, a waveguide had to be defined as singlemode (SM) or multimoded (MM). For this purpose, the laser light was input to the waveguides in an off-axis position to excite possible higher order modes. Images

<i>Sample#</i>	$H(\mu\text{m})$	$w(\mu\text{m})$	$h(\mu\text{m})$	$e(\mu\text{m})$	w/H	h/H	Mode
SMSOI01	3	3	2.3	0.7	1	0.77	SM
SMSOI02	3	3	2.31	0.69	1	0.77	SM
SMSOI03	4	3	1.68	2.32	0.75	0.42	MM
SMSOI05	3	4	2.04	0.96	1.33	0.68	MM
SMSOI06	3	3	2.29	0.71	1	0.76	SM
SMSOI07	4	3	2.6	1.4	0.75	0.65	SM
SMSOI09	3	5	2.67	0.33	1.67	0.89	SM
SMSOI10	5	5	3.41	1.59	1	0.68	MM
SMSOI11	4	5	3.47	0.53	1.25	0.87	SM
SOIMMI01	5	3	3.3	1.7	0.6	0.66	SM
SOIMMI03	5	3	2.91	2.09	0.6	0.58	MM
SOIMMI05	5	3	3.0	2.0	0.6	0.6	SM

Table 4.2: The geometrical dimensions of analyzed SOI optical waveguides.

of waveguide modes were then captured. TE and TM fundamental modes of a single mode waveguide is given in Fig.10. Also, the images of output port when input port is off-axis aligned with input light are shown in Fig.4.11. Here both fundamental(Fig.4.11c) and first excited mode(Fig.4.11a) of a SOI optical waveguide is seen.

As a result, the single mode condition for rib waveguide proposed by Soref *et.al.* and enhanced by Pogossian *et.al.* was verified by BPM simulations and experimental results. It can be stated that the single mode condition for rib waveguides is a very useful and practical way of designing single mode waveguides.

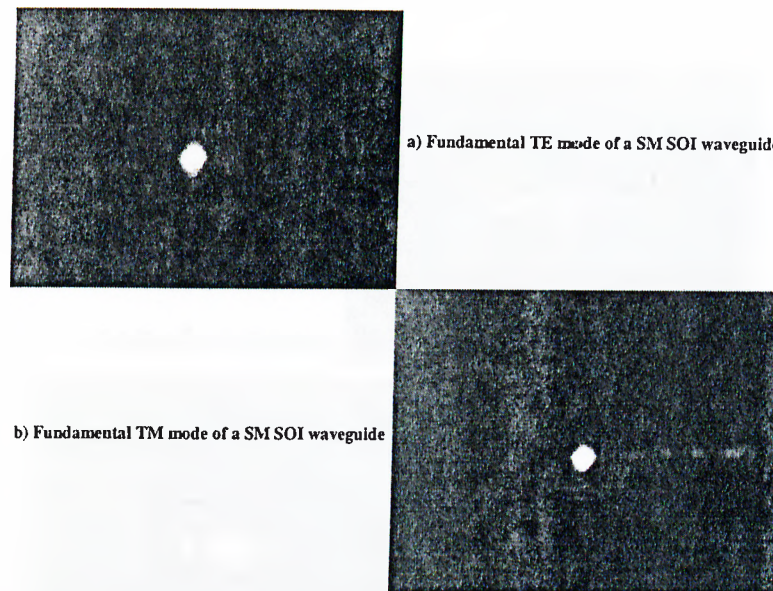


Figure 4.10: TE and TM fundamental modes of a single mode waveguide on sample SMSOI09.

4.2.3 Optical Waveguide Loss Measurement

Some of the fabricated SM SOI waveguide samples was used for optical loss measurements. Initially, we tried Fabry-Perot interference method to measure propagation loss. However, the results were not encouraging. This method requires optically cleaved and parallel waveguide facets which behave as partially reflecting mirrors. These conditions were partially met by our fabricated SOI waveguides. To get optically cleaved facets was difficult and was possible only for a few of the SOI waveguides on a sample after cleavage. Two kinds of waveguide facets resulted in a cleavage process. If the cleavage is not perfect enough few of the waveguide facets were fine while the most were not good enough for optical measurements. The second kind of facets that we obtained resulted according to definition of a perfect cleavage. The waveguides had broken and sloped rib facets while the slab layer of the waveguide is vertical (see Fig.4.12). The waveguides with facets of the first kind was found to be good for optical measurements. However, it was almost impossible to couple light to waveguides with facets of

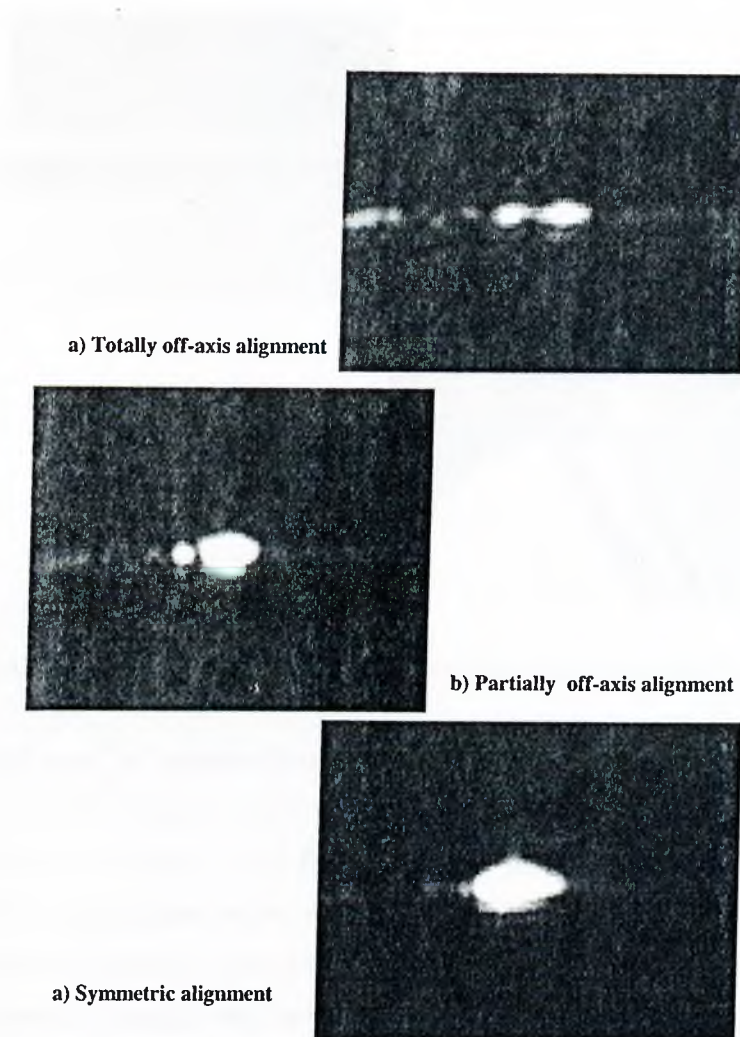


Figure 4.11: Output images of an output port of SOI waveguides on sample SOIMMI05 with different alignments.

second kind (optically cleaved but with broken and sloped rib). Despite the fact that, cleaving a sample was made possible by backside thinning sloped ribs formed during cleavage caused problems during light coupling. We have not yet found a reasonable explanation for this mechanical problem of sloped rib formation.

We, therefore, decided to use butt coupling along with by cut-back method for optical loss characterization of the waveguides. Samples of several millimeters

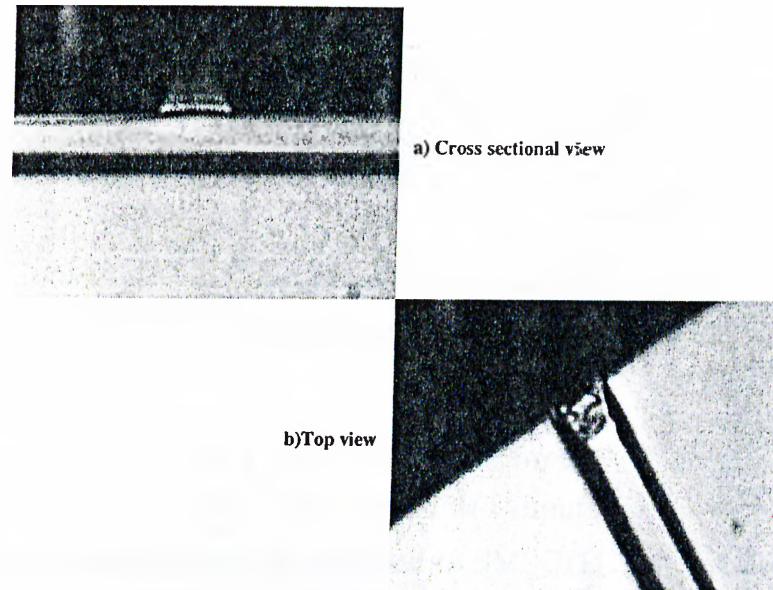


Figure 4.12: Sloped rib facets after a standard optical quality cleavage.

long were first used in measurements then they were successively cleaved into asymmetric lengths. These shorter waveguides were also used in measurements. To find total input power, a SM fiber carrying laser light was brought to the focus point of a microscope objective and optical power was directly measured by a Ge detector attached to an optical powermeter. The power value measured when the waveguide sample was between the SM fiber and microscope objective is output power. Output powers of 5-10 waveguides were averaged for each waveguide length. The measured optical powers were then expressed in terms of dB. What is found in this kind of loss measurements is *insertion loss* which includes propagation loss and losses due to fiber to waveguide coupling at input and output facets. The measured typical insertion losses for analyzed samples are given in Table 4.3. as can be seen TE and TM insertion losses are comparable within the measurement error. Furthermore, it is clearly seen that the insertion losses decrease as the cross sectional area of the waveguides increases. This is due to better coupling of light in and out of the waveguides. The measured best values which were not added to above typical values came out to be

<i>Sample#</i>	TE loss (dB)	TM loss (dB)
SMSOI01	20.9	21.9
SMSOI02	22.3	21.7
SMSOI11	19.7	19.8
SOIMMI01	16.6	16.8

Table 4.3: Typical measured insertion losses.

$$\begin{aligned}
 &12.2 \text{ dB for } TE \text{ input.} \\
 &12.7 \text{ dB for } TM \text{ input.}
 \end{aligned}
 \tag{4.1}$$

Furthermore, cutback method was applied to SMSOI11. The initial 11 mm long sample was cleaved into two pieces of 7.5 mm and 3.5 mm long, after the first loss measurement. The measurements were repeated for the new shorter waveguides. The loss values were plotted in Fig.4.13 as a function of waveguide length. Linear fit to the measured data gave the propagation loss values about

$$\begin{aligned}
 &0.70 \pm 3.4 \text{ dB/cm for } TE \text{ input.} \\
 &0.76 \pm 3.7 \text{ dB/cm for } TM \text{ input.}
 \end{aligned}
 \tag{4.2}$$

The propagation losses deduced from measured insertion losses are close to the loss values from literature. The reported loss values range from 0.1 dB/cm¹⁹ to 2dB/cm.²³ It should be noted that, the 0.1 dB/cm loss was measured for SOI rib waveguides with cross sections as large as 11 μm . While, 2 dB/cm value is the loss of waveguides of 3 μm cross section. Also, the errors for reported values are in the range of ± 0.1 dB/cm to ± 0.6 dB/cm.⁴⁷ Our propagation loss results seem to support the claim of Zinke *et.al.*²⁰; it is possible to reach losses as low as 0.5 dB/cm with SOI waveguides of cross sections ≥ 4 μm . Also, the low inherent defect density of BESOI wafers and our very smooth waveguide walls explain the measured loss values. The loss values can be further improved, if waveguides with larger cross sections are fabricated and measured.

As far as insertion loss considered, it can be stated that the relatively high losses are mainly due to the poor coupling at waveguide facets. This statement is

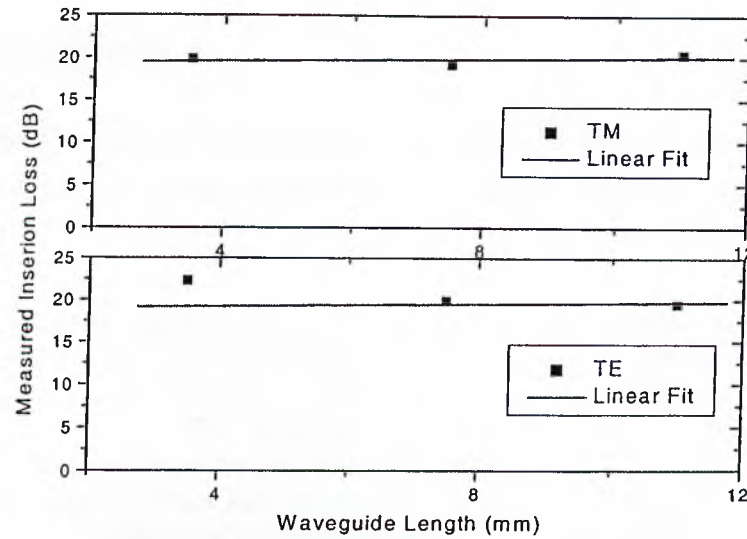


Figure 4.13: Measured insertion losses versus waveguide length.

confirmed by our loss measurement results since, the propagation loss is low and shortening the waveguides did not lead a major improvement in insertion loss. The reported insertion losses are between 3 dB and 9.6 dB for waveguide various cross sections.¹⁸ Improving insertion loss seems to be one of the first thing to do in our near future plans. For this purpose, better waveguide facets are needed. Some ideas are already under consideration. The first is that waveguide facets may be chemomechanically polished. This process may supply optical quality facets, but paralleling of facets can not be guaranteed and requires proper equipment which is not yet available. Parallel facets is not a must for improving insertion loss but is needed if Fabry-Perot technique is to be applied. The second possibility is that waveguide facets may be defined by a reactive ion etching (RIE) prior to sample cleavage. This process is expected to result in both optically cleaved and parallel waveguide facets if the process is well optimized.

4.3 Characterization of Optical Directional Couplers

SOI directional couplers were fabricated on samples from Wafer 1. The sample characterized had the geometrical dimensions given in Table 4.4.

Waveguide Height, H	3 μm
Waveguide Width, w	3 μm
Slab Height, h	2.35 μm
Gap between two straight sections, g	3.25 μm
Gap between two inputs or outputs	29 μm
Straight section lengths	1250-4250 μm

Table 4.4: Geometrical dimensions of the characterized directional couplers

The same optical measurement setup on which the waveguide loss measurements were performed had also been used for directional couplers. The directional couplers were identical except their straight section lengths. The DFB laser light was butt coupled to one of the inputs of a coupler from a SM fiber. Then, the light from both bar and cross outputs was visualized by a TV monitor attached to the IR camera. The fiber-input waveguide coupling was optimized for better imaging. The images were then captured using the TV card integrated to a PC as explained in section 4.2.1. Care was taken to make such that the IR camera was not saturated by using neutral density filters. Another image was captured, while light coupled into the other input. The same procedure explained above for one coupler pair was applied to all other couplers on the same sample for both TE and TM polarized input light. Three of the captured images of couplers with different straight section lengths for TE polarized light input are given in Fig.4.14. Here the light was input at the right port. Fig.4.14a shows full coupling while in Fig.4.14b a nearly half coupling (3 dB) is seen.

The captured images were analyzed by a computer program, *Scion Image*. This program was used to find the intensities of both bar and cross outputs

for each captured image. Examples of these peak profiles also can be seen in Fig.4.14 for each image. Ratios of intensities of bar or cross outputs to total output intensity were calculated, by also considering that the IR camera gives intensities which are square root of the real ones. These so-called coupling ratios were then plotted as a function of straight section lengths (see Fig.4.15). The curves resulted from fitting

$$\frac{I_{Cross}}{I_{Total}} = \sin^2\left(\frac{L}{L_c}\right) \quad (4.3)$$

which can be shown using Eqs. 2.33 and 2.34 of Chapter 2, are also given in Fig.4.15.

Coupling lengths deduced from this fitting are

$$\begin{aligned} L_c &= 1353\mu m \text{ for } TE \text{ input.} \\ L_c &= 1916\mu m \text{ for } TM \text{ input.} \end{aligned} \quad (4.4)$$

As can be seen in Fig.4.14, full coupling takes place when straight section length is nearly 1250 μm , but fitting results in coupling length of 1353 μm for TE polarization. This difference can be explained by the existence of s-bends at both beginning and end of the straight sections. S-bends are used to be able to input light into only one of the input ports from a SM fiber and they come very close to each other to let light propagate to straight sections. Therefore, light coupling starts before straight sections and continues after straight sections where s-bend sections come very close to each other. So, it can be said that the coupling lengths given in Eq. 4.4 are the effective coupling lengths and can not be directly related to the straight section lengths.

This explanation is also verified by the BPM simulations of the measured couplers. First, straight sections of dimensions given in Table. 4.4 were used in simulations, the results are given in Fig.4.16. From the coupling ratio plots coupling lengths are found to be around

$$\begin{aligned} L_c &= 1600\mu m \text{ for } TE \text{ input.} \\ L_c &= 1800\mu m \text{ for } TM \text{ input.} \end{aligned} \quad (4.5)$$

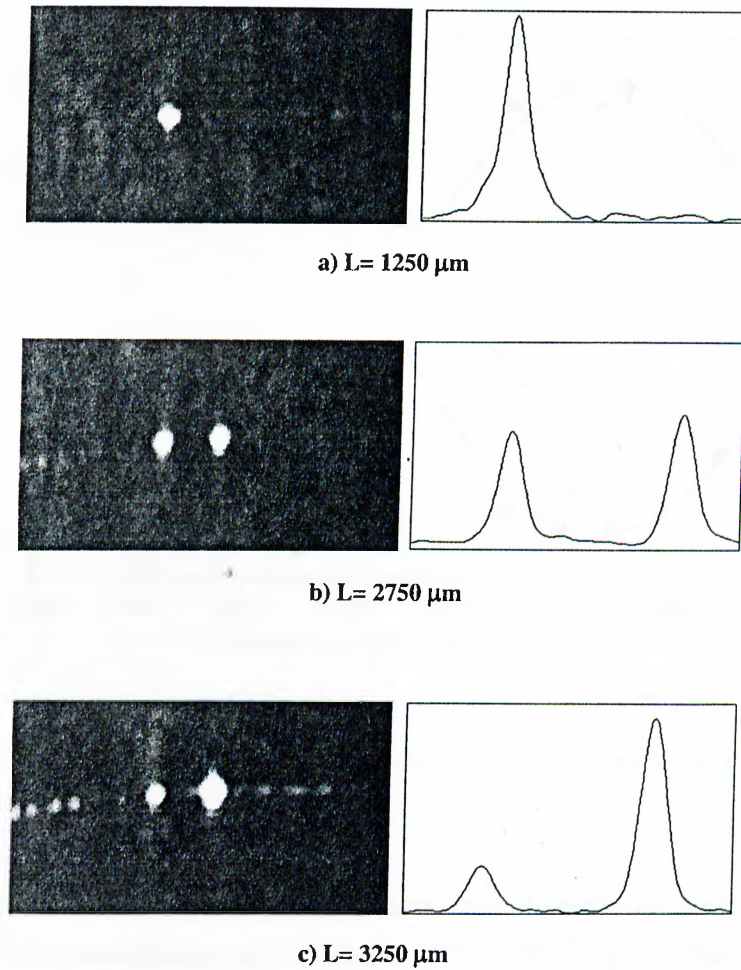


Figure 4.14: Output images and peak profiles at different straight section lengths(L).

The values resulted from this simulations are comparable with those resulted from fitting to measurement results (given in Eq. 4.4). Then, simulations for the characterized couplers were repeated with s-bends included this time. S-bends used in simulations were composed of two bends with radius of 5 mm and length of 300 μm , which are chosen to be similar to their counterparts on the coupler mask. These simulations gave exactly the same result as obtained in

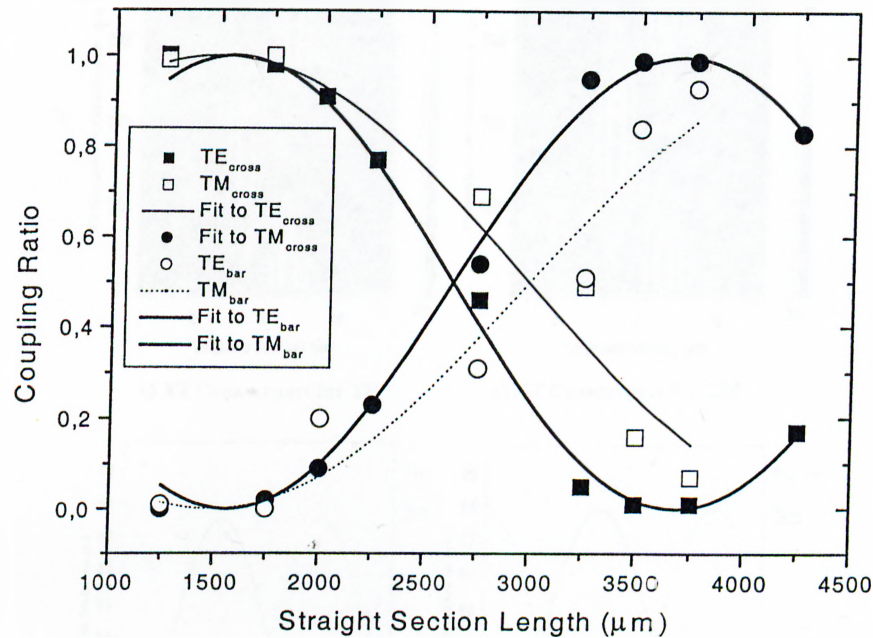


Figure 4.15: Coupling ratios and fitting curves for the characterized couplers.

measurement (see Fig.4.17).

In conclusion, we fabricated and characterized directional couplers based on single mode SOI waveguides at a wavelength of $1.55 \mu\text{m}$. The measurement results are shown to be confirmed by BPM simulations. The difference between coupling lengths for TE and TM polarized light can be understood by recalling that the effective index difference between the rib section and the slab section of the SOI optical waveguides is larger for the TE polarization, this leads a larger coupling constant so to a shorter coupling length. Relatively high confinement of SOI rib waveguides requires straight sections be closer to each other for shorter coupling lengths. For example, in our structure with waveguide separation of $3.25 \mu\text{m}$, 3 dB couplers seem to be possible at the straight section length of about $625 \mu\text{m}$. While, it has been reported that 3 dB SOI couplers has been realized at straight section lengths of $400 \mu\text{m}$ with $2.5 \mu\text{m}$ waveguide separation.²⁵ Finally, it should be stated that the understanding of directional couplers is important

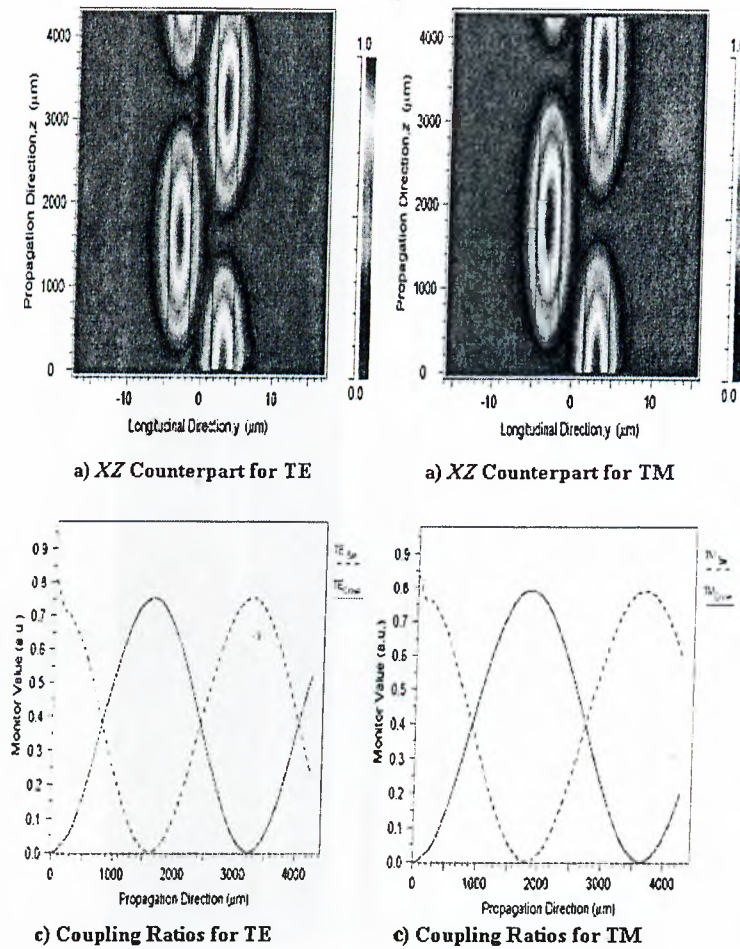


Figure 4.16: BPM simulation results of straight sections only: XZ counterparts and coupling ratios for both TE and TM, $L=4250 \mu\text{m}$.

before realization of certain integrated optical devices and circuits, such as wavelength division-multiplexed (WDM) networks based on Mach-Zehnder type interferometry.

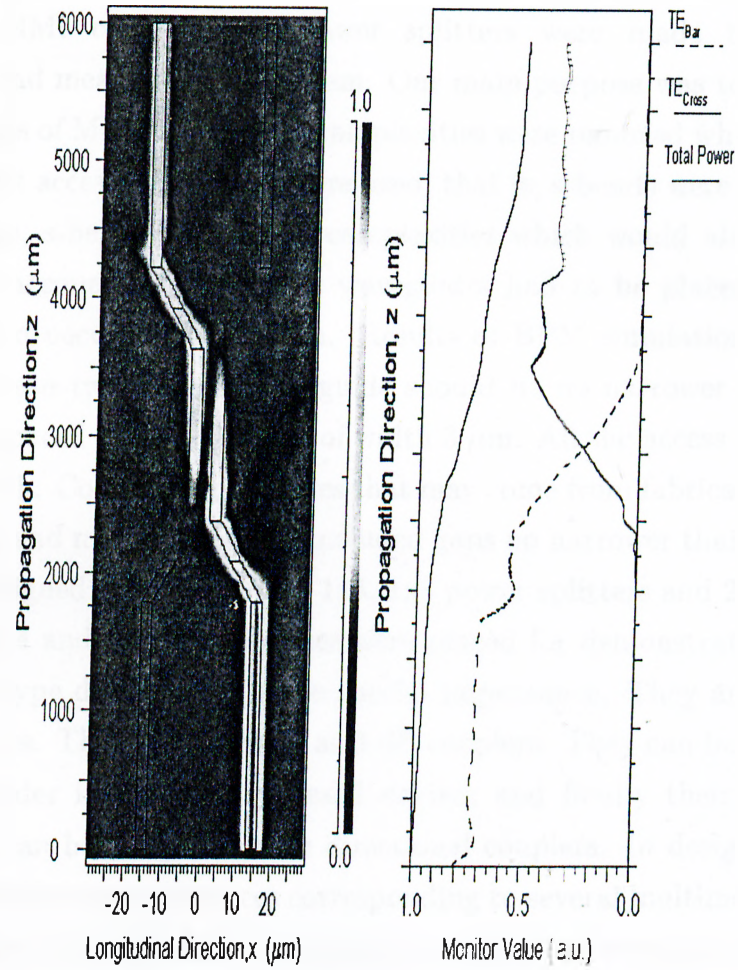


Figure 4.17: BPM simulation results, s-bends included: XZ counterpart and coupling ratios for TE and $L=1250 \mu\text{m}$.

4.4 Characterization of Optical MMI Couplers

There were no available MMI masks, so we designed our own mask. The details are given below, and the results of the measurements are presented.

4.4.1 The Mask Design

Design of MMI couplers and power splitters were made to have simple fabrication and measurement for them. Our main purpose was to observe major characteristics of MMI couplers, so complexities were removed whenever possible. Thus, straight access waveguides were used, that is, s-bends were not used in the design. Since, s-bends bring some complexities which would also be necessary to take into account. These access waveguides had to be placed such that no coupling could occur between them. Results of BPM simulations showed that the gap between two straight waveguide should be no narrower than $8 \mu\text{m}$ for two parallel spaced SOI waveguides of width $3 \mu\text{m}$. All the access waveguides are with this width. Considering mistakes that may come from fabrication and for an easier testing and measurement we included gaps no narrower than $15 \mu\text{m}$ on the mask. We designed and placed 1x2, 1x4, 1x8 power splitters and 2x2 couplers on the mask. 1X4 and 1X8 type devices were placed for demonstration. However, 1x2 and 2x2 type devices have some special importance. They are the simplest MMI structures. They are designed as 3-dB couplers. They can be easily applied to Mach-Zehnder interferometry based devices and finally their performances and function can be compared with directional couplers. In design of the MMI couplers, multiple image distances corresponding to several multimode waveguide section widths were calculated according to results of section 2.4 for general interference, then BPM simulations were performed for these structures and optimum lengths for 2-fold, 4-fold and 8-fold images were found (See Figs.4.18 and 4.19 for some BPM simulation results). As can be in the figures showing simulation results, N-fold image length corresponds the length at which the electric field distribution has N maximums. Also, for a definite MMI width 4-fold and 8-fold images are formed at shorter lengths, but the gap between access waveguides becomes to small to avoid coupling between waveguides. So, 1x2, 1x4 and 1x8 MMI power splitters were designed with different MMI widths ensuring no coupling between access waveguides. The details of the MMI structures on the mask is seen in Table 4.5. The designed MMI couplers were like those seen in Fig.2.12.

Type	W_{MMI} (μm)	Gap, g (μm)	Acc. WG width(μm)	L_{MMI} (μm)
1x2	48	21	3	2750
1x2	64	29	3	4850
2x2	36	15	3	2275
2x2	48	21	3	3960
2x2	64	29	3	5010
1x4	88	19	3	4485
1x4	128	21	3	9045
1x8	168	18	3	8100
1x8	200	22	3	11410

Table 4.5: List of MMI structures on the designed mask.

Table 4.5 does not show all the devices on the mask. Apart from those shown in the table, devices with various MMI section lengths were also included for each device group. The lengths of the extra devices were decided considering the length tolerance (see section 2.5) value for SOI structure which was estimated to be $16 \mu\text{m}$. So devices with length $L_{MMI} \pm 16q \mu\text{m}$, where q is an integer, were also placed on the mask. These extra devices are for the possible design and fabrication tolerance tests.

4.4.2 Measurements and Results

The same measurement setup and procedure used in measurement of directional couplers were employed for MMI couplers. That is, captured images were analyzed with Scion image analyser software. In measurement, 1x2 and 2x2 devices were analyzed for their outputs under both TE and TM polarized light. All devices were demonstrated to be working and their output pictures are given in later parts of this section. Insertion loss (called excess loss for 3 dB couplers) and splitting ratio (unbalancing) are the parameters which can be analyzed with respect to the variations in MMI couplers geometrical dimensions (MMI width and MMI length). This analysis can be done under different states of polarization and for varying wavelength. So, the MMI length and width tolerance, polarization

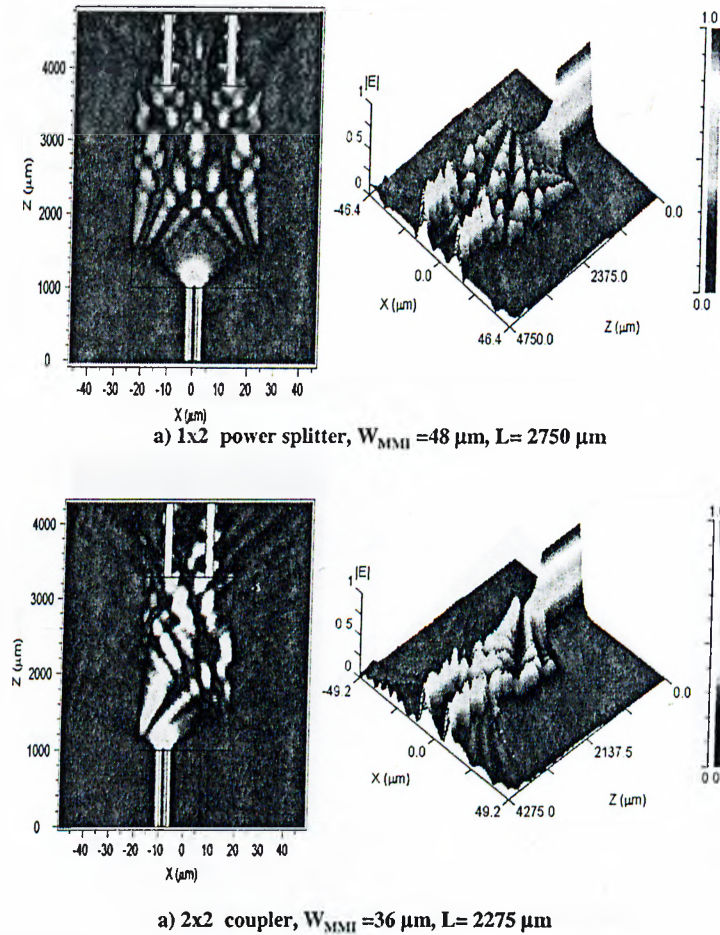


Figure 4.18: BPM simulation results for 1x2 MMI power splitters and 2x2 MMI couplers.

sensitivity and optical bandwidth for a designed coupler can be evaluated.

Our designed MMI couplers let us only test the parameters with respect to variation in MMI lengths under both TE and TM polarization. Bandwidth measurements requires a tunable laser light source which was not available. Due to the facet problems explained in section 4.2.3, unbalancing of all the fabricated devices could not be analyzed as a function of MMI section length. However, 1x2

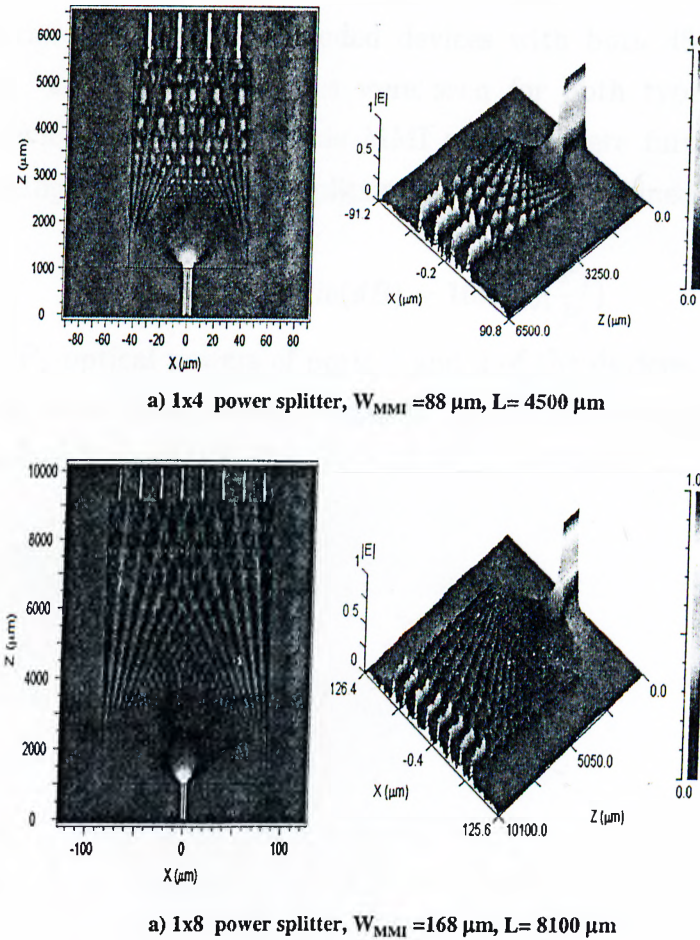


Figure 4.19: BPM simulation results for 1x4 and 1x8 MMI power splitters.

and 2x2 types were analyzed despite this problem. Insertion losses were measured to be around 27.5 dB for TE and 29 dB for TM polarized input light. These relatively high insertion losses are understood to be due to the facet problems and also radiation losses in regions especially where MMI sections and access waveguides connect. The radiation losses are clearly seen in BPM simulation results. The results for each device group are given one by one.

1x2 MMI Power Splitters

The characterized 1x2 sample included devices with both 48 μm and 64 μm MMI widths. 2-fold output images were seen for both type of devices (see Fig.4.20). Devices with 48 μm wide MMI sections were further analyzed for their unbalancing, splitting ratio. Splitting ratio can be defined as

$$\text{SplittingRatio}(dB) = 10\log_{10}\left(\frac{P_1}{P_2}\right) \quad (4.6)$$

where P_1 and P_2 optical powers of ports 1 and 2 of the devices. The results are given as a function of MMI section length in Fig.4.21. The measured best value of splitting ratio is around 0.5 dB.

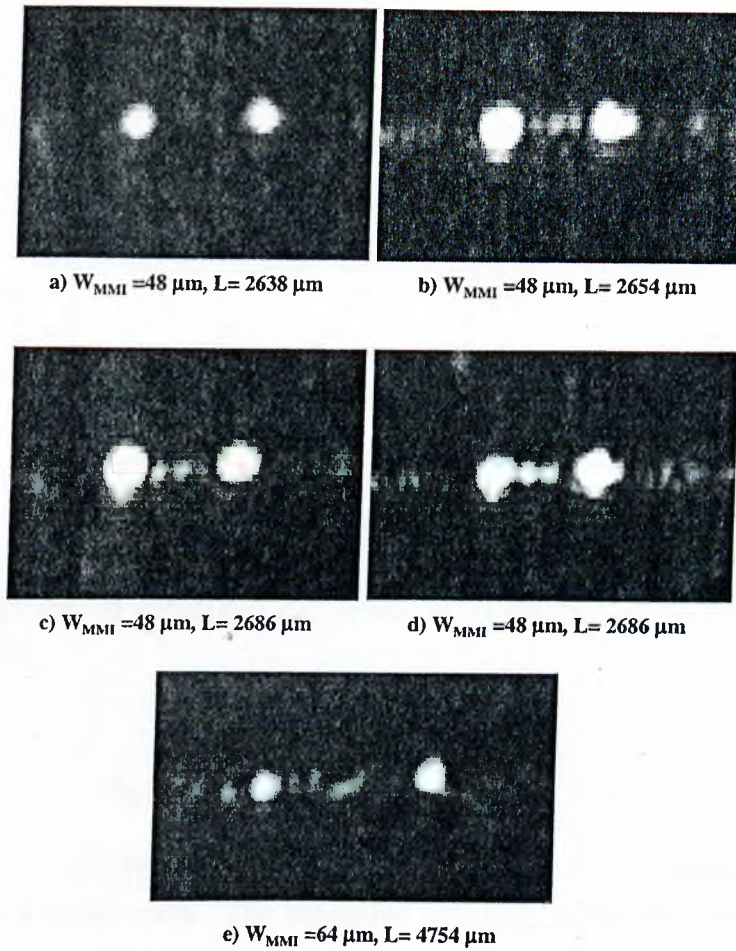


Figure 4.20: Output port images of 1x2 MMI power splitters for various MMI section lengths .

2x2 MMI Couplers

There was 2x2 devices of three different MMI section widths, $36 \mu\text{m}$, $48 \mu\text{m}$ and $64 \mu\text{m}$, on the measured sample. The 2-fold output images were observed for all three types. Images can be seen in Fig.4.22. The splitting ratio is also an parameter for 2x2 MMI 3 dB couplers. It is now defined as

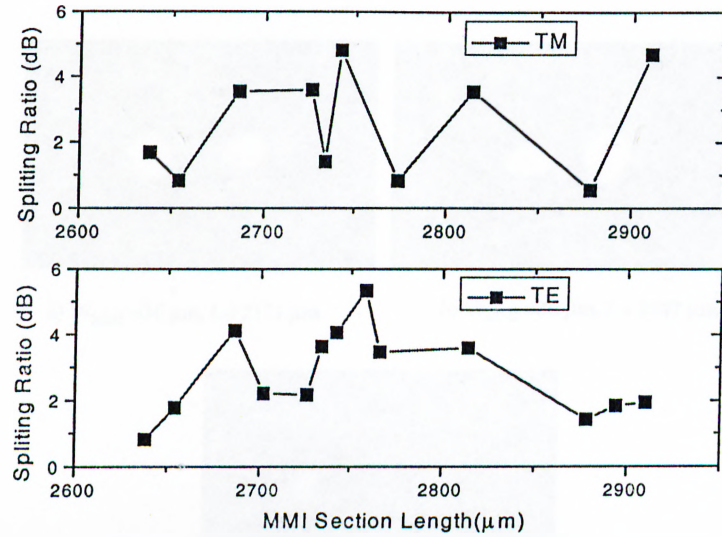


Figure 4.21: Measured splitting ratio versus MMI section length for 1x2 devices of 48 μm width.

$$SplittingRatio(dB) = 10\log_{10}\left(\frac{P_{Bar}}{P_{Cross}}\right) \quad (4.7)$$

which is similar to the previous equation, but the sign of the value is decided by defining bar and cross ports. The measured splitting ratios with best values as low as 0 dB (totally inbalance) are presented in Figs.4.23 and 4.24.

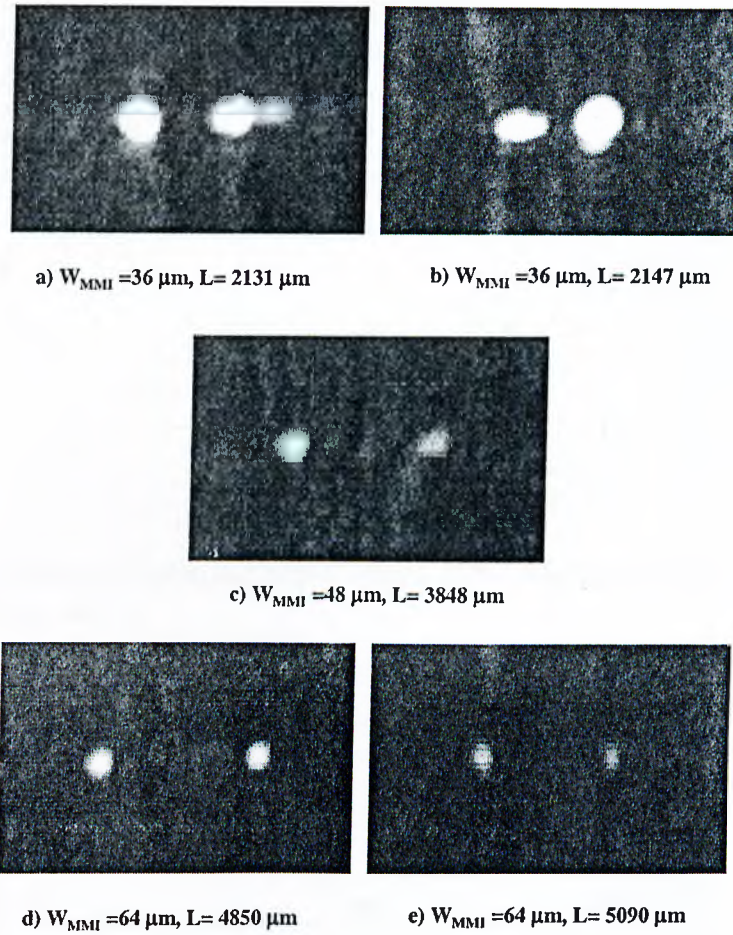


Figure 4.22: Output port images of 2x2 MMI couplers for various MMI section lengths .

1x4 and 1x8 MMI Power Splitters

Only, preliminary measurements were performed 1x4 and 1x8 MMI power splitters and 4-fold and 8-fold images were observed. Images of observed outputs are given in Fig.4.25. Further characterization is planned to be done in near future.

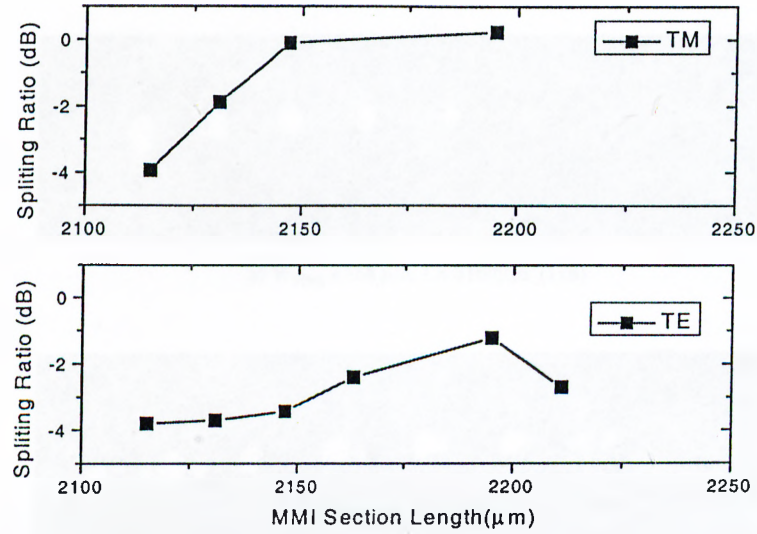


Figure 4.23: Measured splitting ratio versus MMI section length for 2x2 MMI couplers of 36 μm width.

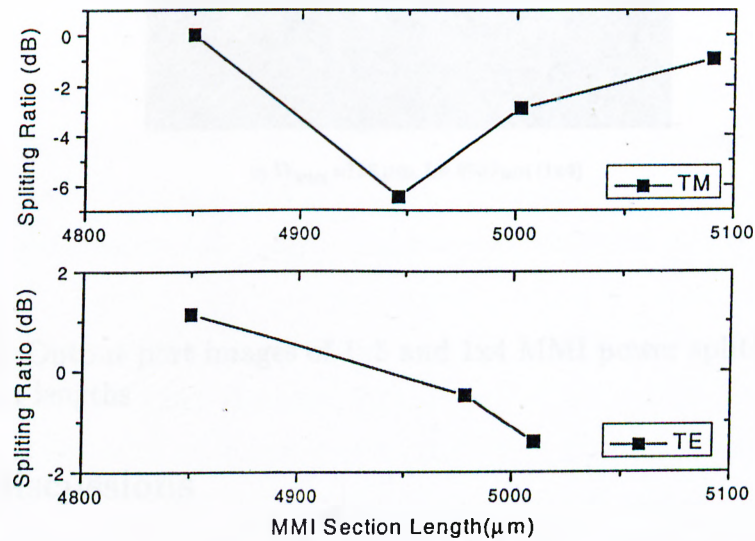


Figure 4.24: Measured splitting ratio versus MMI section length for 2x2 MMI couplers of 64 μm width.

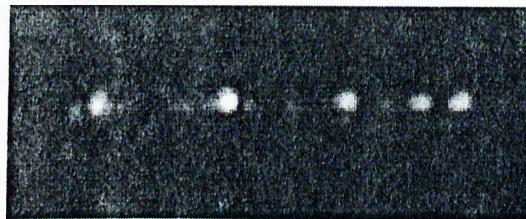
a) $W_{\text{MMI}} = 168 \mu\text{m}$, $L = 8100 \mu\text{m}$ (1x8)b) $W_{\text{MMI}} = 168 \mu\text{m}$, $L = 8180 \mu\text{m}$ (1x8)c) $W_{\text{MMI}} = 128 \mu\text{m}$, $L = 8917 \mu\text{m}$ (1x4)

Figure 4.25: Output port images of 1x8 and 1x4 MMI power splitters for various MMI section lengths .

4.4.3 Discussions

1x2, 2x2 and 1x8 power splitters and 2x2 MMI 3 dB couplers have been designed and fabricated facilitating multimoded SOI waveguides. Despite the difficulties emerging from poor waveguide facets, all the MMI devices were demonstrated to be working. This shows that the MMI design tools used, a mode propagation method based on effective index method along with BPM simulations have worked

well. As far as splitting ratio is concerned, we measured good values (around 0.5 dB) for 1x2 MMI power splitters and very good values (0 dB) for 2x2 MMI couplers. Reported splitting ratio values are around 0.2 dB,³⁵ all with MMI lengths shorter than 600 μm . The measured splitting ratios values around 4 dB can be understood as follows. First of all, it was shown with Eq. 2.51 of section 2.5 that the shorter MMI lengths allows higher tolerance. So, it is natural to expect lower tolerance in general and higher splitting ratios in particular when the device length is large. Also, higher splitting ratios may result from measurement errors. For example, different waveguide facet qualities for output ports of a device may give higher but wrong splitting ratios. It should be also noted that very different output facet qualities introduces higher error limits for splitting ratios. It is known that MMI couplers are not so polarization sensitive. We observed that this is generally so, but with some scattered data points which is most probably due to the reasons just explained. After experience with design, fabrication and testing of both directional coupler and 2x2 MMI coupler, it can be stated that design and fabrication of MMI couplers are more simpler and it is possible to reach shorter 3 dB MMI couplers with higher fabrication tolerance and lower polarization sensitivity. Whereas, the coupling length of directional couplers strongly depends on transverse dimension of waveguides, which observed both during simulation and measurements. MMI couplers are not so dependent on transverse dimensions as long as single mode condition is satisfied for access waveguides.

The MMI structures and mainly 3 dB power splitters and couplers find application in Mach-Zehnder structures. The design, fabrication and demonstration of MMI couplers presented in this thesis has been very useful for our future plans about MMI coupler based devices and systems, especially Mach-Zehnder structures. The experience with simple structures is needed before going on with more complex structures. For example, it was shown that splitting ratios even around 0.2 dB might be critical for extinction ratio of the fabricated devices.³⁵ We believe that with better waveguide facets, measured splitting ratio results would be better.

Chapter 5

Conclusions and Discussions

This thesis work presents the first part of the effort to develop a library of silicon-on-insulator (SOI) optical integrated devices operating at wavelength of $1.55 \mu\text{m}$. In this part SOI single mode waveguides, directional couplers and a number of MMI couplers were designed, simulated, fabricated and characterized.

Effective index method and the single mode condition for rib waveguide proposed by Soref *et.al.* and enhanced by Pogossian *et.al.* (Eqs. 2.20 and 2.21) has been used for design of SM waveguides. BPM simulations were performed for all the fabricated devices. Waveguides and other devices were defined on SOI samples by wet etching in KOH solutions. Solvents (KOH, H₂O and ISO) ratio and other etching parameters were optimized for the smoothest surface and rib side walls. Characterization of fabricated devices requires optically cleaved samples, which was impossible for SOI samples as thick as $525 \mu\text{m}$. This problem was partially resolved by backside thinning of samples for which device fabrication was over. In thinning process, we again made use of a KOH solution. The cleavages allowed optical measurements. Fabricated and cleaved device samples were characterized on a standard fiber optic measurement setup.

A number of SOI waveguide samples had been fabricated and characterization results were used to evaluate the single mode condition. It was found that, measurements and BPM simulations gave results which perfectly fit to the SM condition. First a number of SOI rib waveguide structures with different

waveguide parameters (width, w , height, H and slab height, h) were chosen. Some of these structures correspond to multimode (MM) waveguides while the others to SM ones, according to SM condition. BPM was then used to simulate some of these structures. In BPM simulations transverse mode profiles of these waveguides were computed. These profiles were then analyzed to determine those which were SM or MM. After that, a number of SOI rib waveguides with different w/H and h/H ratios were fabricated and their modal properties were analyzed on the optical measurement setup. Experimental results show a behaviour totally in line with the single mode condition and BPM simulations. It has been shown that the single mode condition for rib waveguides is a very useful and practical way of designing single mode waveguides.

Single mode waveguide samples were used in optical loss measurements. Initially the Fabry-Perot interference method did not give encouraging results. Optically cleaved and parallel waveguide facets which were required in this method were partially met by our fabricated SOI waveguides. Due to explained facet problems (not optically cleaved facets and broken and sloped facets), butt coupling along with the cut-back method was used for optical loss characterization of the waveguides. Long samples were first used in measurements then they were successively cleaved into asymmetric lengths and insertion loss measurements were repeated for these shorter samples. Measured insertion loss includes propagation loss and losses due to fiber to waveguide coupling at input and output facets. The measured insertion losses have average values between 16.6 to 22.3 dB for TE and 16.8 to 21.9 dB for TM polarized light. The best measured value for TE was as low as 12.2 dB and that for TM comes as 12.7 dB.

The propagation losses, 0.70 dB/cm for TE and 0.76 dB/cm for TM, deduced from measured insertion losses are around the loss values from literature. Loss values range from 0.1 dB/cm¹⁹ to 2 dB/cm²³ had been reported. The errors for reported values are in the range of ± 0.1 dB/cm to ± 0.6 dB/cm.⁴⁷ Our propagation loss results are in accordance with the claim of Zinke et.al.²⁰; it is possible to reach losses as low as 0.5 dB/cm with SOI waveguides of cross sections $\geq 4 \mu\text{m}$. Also, the low inherent defect density of BESOI wafers and our

very smooth waveguide walls explain the measured loss values.

It is clear that coupling losses at input and output of waveguides were the major part of the measured insertion losses. This can be confirmed by our loss measurement results. The propagation loss is low and shortening waveguides did not lead a major improvement in insertion loss. Improving insertion loss seems possible since the insertion losses between 3 dB and 9.6 dB for waveguide various cross sections¹⁸ had been reported. For this purpose, better waveguide facets should be obtained. Some of the processes that can help are chemomechanically polishing waveguide facets and defining facets by a reactive ion etching (RIE). A new idea recently discussed is to deposit a oxide layer of as thick as a few microns over the fabricated waveguides and then perform cleavage, this deposited upper cladding may avoid the formation of broken and sloped ribs during cleavage.

The characterized directional couplers were found to have coupling lengths of 1353 μm for TE and 1916 μm for TM polarized light. However, full coupling was observed for straight section length of 1250 μm . This difference was understood as follows: Coupling in directional couplers starts in s-bends and this shortened the required straight section length for full coupling. S-bends are used to be able to input light into only one of the input ports from a SM fiber and they come very close to each other to let light propagate to straight sections. Therefore, light coupling starts before straight sections and continues after straight sections where s-bend sections come very close to each other. Therefore, it should be noted that the coupling lengths found from fitting to result of measurements are the effective coupling lengths and not the straight section lengths.

The difference between coupling lengths for TE and TM polarized light was understood within the effective index knowledge of both states of polarization. High confinement of SOI rib waveguides requires closely spaced straight sections for shorter coupling lengths. For example, in our structure with waveguide separation of 3.25 μm , 3 dB couplers seem to be reachable at the straight section length of about 625 μm . While, it had been reported that 3 dB SOI couplers had been realized at straight section lengths of 400 μm with 2.5 μm waveguide separation.²⁵

A mode propagation method based on effective index method along with BPM simulations have been used in design of the MMI couplers. The designed mask included 1x2, 1x4 and 1x8 MMI power splitters and 2x2 MMI couplers with various MMI widths and lengths. Straight waveguides are used as access waveguides, this requires wider MMI devices to place access waveguides such that no coupling occur between them. So, long devices resulted after the design. Optimum lengths for a definite MMI width are the distances at which electric field has N maxima. N -fold images are formed at this length. Lengths around the optimum values were also included for possible tolerance analysis. Insertion losses which come to be around 27.5 dB for TE and 29 dB for TM and splitting ratios were measured. The insertion losses seem reasonable when compared to the straight waveguides. The facets became source of problem here, also. However, all devices were demonstrated to be working.

1x2 and 2x2 type devices were analyzed for their splitting ratios. The best measured values came to be around 0.5 dB for 1x2 power splitters and 0 dB for 2x2 couplers which is very good. Some of the data points showing higher values are considered to be due to both long MMI lengths and errors resulting from possible different facet qualities of outputs of a device. The splitting ratio of MMI couplers are polarization insensitive in general. As far as MMI couplers compared to directional couplers, it can stated realization of 3 dB MMI couplers with higher fabrication tolerance and lower polarization sensitivity is simpler.

Finally, we have the technology and experience to design, fabricate and test most of the integrated optical devices on SOI wafers. However, we need to find and optimize a process to get good waveguide facets. The proposed methods are expected to solve this problem in the near future.

Bibliography

- [1] J. Singh, "Semiconductor Optoelectronics", New York:McGraw-Hill, inc., (1995)
- [2] R. G. Hunsperger, "Integrated Optics", Berlin: Springer-Verlag, (1995)
- [3] T. Tamir, "Integrated Optics", Berlin:Springer, (1979)
- [4] S. E. Miller, A. G. Chynoweth, "Optical Fiber Communications", New York:Academic (1979)
- [5] G. Giesecke "Lattice Constants: Semiconductors and Semimetals 2", New York:Academic (1976)
- [6] R. Marz, "Integrated Optics", Boston:Artech Hause, Inc., (1995)
- [7] L. D. Hutcheson, "Integrated Optical Circuits and Components", New York:Marcel Dekker, Inc., (1987)
- [8] B. Jalali, S. Yegnanarayanan, T. Yoon, T. Yashimoto, I. Rendina, and F. Coppinger "Advances in Silicon-on-Insulator Optoelectronics", IEEE Journal of Selected Topics in Quantum Electronics, 4:6, (1998)
- [9] T. Miya "Silica-Based Planar Lightwave Circuits: Passive and Thermally Active Devices ", IEEE Journal of Selected Topics in Quantum Electronics, 6:1, (2000)
- [10] R. Germann, H. W. M. Salamink, R. Beyeler, G. L. Bona, F. Horst, I. Massarek and B. J. Offrein "Silicon-Oxynitride Layers for Optical Waveguide

- Applications", IBM Research Report, Engineering and Technology, **RZ 3102:93147**, (1999)
- [11] R. A. Soref and J. P. Lorenzo, "All-silicon Active and Passive Guidedwave Components", *IEEE Journal of Quantum Electronics*, **22:p873**, (1986)
- [12] A. Splett and K. Petermann "Low Loss Single Mode Optical Waveguides with Large Cross-section in standard Epitaxial Silicon", *IEEE Photonics Technology Letters*, **6:p425**, (1994)
- [13] A. Splett, J. Schmidtchen, B. Schuppert, K. Petermann, E. Kesper and H. Kibbel, "Low Loss Optical Ridge Waveguides in Strained GeSi Epitaxial Layer Grown on Silicon", *Electronics Letters*, **26:p1035**, (1990)
- [14] R. A. Soref, F. Namavar and J. P. Lorenzo, "Optical Waveguiding in a Single-Crystal Layer of Germanium Silicon Grown on Silicon", *Optics Letters*, **15:p270**, (1990)
- [15] R. A. Soref, F. Namavar, "Optical Waveguiding in Ge_xSi_{1-x}/Si Heterostructures", *Journal of Applied Physics*, **70:p3370**, (1990)
- [16] S. F. Pesarcik, G. V. Treyz, S.S. Iyer, and J. M. Halbout, "Silicon Germanium Optical Waveguides With 0.5 dB/cm Losses for Single Mode Fiber Optic Systems", *Electronics Letters*, **28:p159**, (1992)
- [17] V. P. Kesan, P. G. May, E. bassous, and S. S. Iyer, "Integrated Waveguide/Photodetector using Si/SiGe Multiple quantum Wells For Long Wavelength Operation", in *IEDM Tech. Dig.*, p1035, (1990)
- [18] B. Schuppert, J. Schmidtchen, A. Splett, U. Fisher, T. Zinke, R. Moosburger, K. Petermann, "Integrated Optics in Silicon and SiGe-Heterostructures", *Journal of Lightwave Technology*, **14:10**, (1996)
- [19] U. Fisher, J. R. Kropp, F. Arndt and K. Petermann, "0.1 dB/cm Waveguide Losses in Single-Mode SOI Rib Waveguides", *IEEE Photonics Technology Letters*, **8:5**, (1996)

- [20] T. Zinke, U. Fisher, A. Splett, B. Schuppert, and K. Petermann, "Comparison of Optical Waveguide Losses in Silicon-on-Insulator", *Electronics Letters*, **29:23**, (1993)
- [21] R. A. Soref, J. Schmidhchen, and K. Petermann, "Large Single-Mode Rib Waveguides in GeSi-Si and *Si - on - SiO₂*", *IEEE Journal of Quantum Electronics*, **27:8**, (1991)
- [22] A. G. Rickman, G.T. Reed, "Silicon-on-Insulator Optical Rib Waveguides; Loss, Mode Characteristics, Bends and Y-junctions", *IEEE Proc.-Optoelectronics*, **141:6**, (1994)
- [23] A. G. Rickman, F. Namavar, "Silicon-on-Insulator Optical Rib Waveguides Loss and Mode Characteristics", *Journal of Lightwave Technology* , **12:10**, (1994)
- [24] R. M. Emmons, B. N. Kurdi, and D. G. Hall "Buried-Oxide Silicon-on-Insulator Structures I: Optical Waveguide Characteristics", *IEEE Journal of Quantum Electronics*, **28:1**, (1992)
- [25] P. D. Trinh, S. Yegnanarayanan, B. Jalali, "Integrated Optical Directional Couplers in Silicon-on-Insulator ", *Electronics Lettres*, **31:24**, (1995)
- [26] P. D. Trinh, S. Yegnanarayanan, B. Jalali, "5x9 Integrated Optical Star Coupler in Silicon-on-Insulator Technology ", *IEEE Photonics Technology Lettres*, **8:?**, (1995)
- [27] P. D. Trinh, S. Yegnanarayanan, B. Jalali, "Guided-Wave Optical Circuits in Silicon-on-Insulator Technology", in *Tech. Dig. Integrated photonics Research Conf.*, Boston **6:page 273-277**, (1996)
- [28] C. Z. Zhao, G. Z. Li, E. K. Liu, Y. Gao and X. D. Liu "Silicon on Insulator Mach-Zehnder Waveguide Interferometers Operating at $1.3 \mu m$ ", *Applied Physics Letters*, **67:17**, (1995)

- [29] G. V. Treyz "Silicon Mach-Zehnder Waveguide Interferometers Operating at $1.3\mu\text{m}$ ", *Electronics Letters*, **27**:2, (1991)
- [30] U. Fisher, T. Zinke, and K. Petermann, "Comparison of Optical Waveguide Losses in Silicon-on-Insulator", *Electronics Letters*, **30**:5, (1994)
- [31] B. L. Weiss, G. T. Reed, S. K. Toh, R. A. Soref, and F. Namavar, "Optical Waveguides in SIMOX Structures", *IEEE Photonics Technology Letters*, **3**:1, (1991)
- [32] R. A. Soref, J. Schmidchen, K. Petermann, "Large Single Mode Rib Waveguides in GeSi-Si and Si-on-SiO₂", *IEEE Journal of Quantum Electronics*, **27**:8, (1991)
- [33] S. P. Pogossian, L. Vescan, and A. Vonsovici "The Single Mode Condition for Semiconductor Rib Waveguides with Large Cross Section", *Journal of Lightwave Technology*, **16**:10, (1998)
- [34] N. Dagli and C. G. Fonstad "Analysis of Rib Waveguides with Sloped Rib Sides", *Applied Physics Letters*, **46**:6, (1985)
- [35] L. B. Soldano, and E. C. M. Pennings "Optical Multi-Mode Interference Devices Based on Self-Imaging: Principles and Applications", *Journal of Lightwave Technology*, **13**:4, (1995)
- [36] R. Ulrich and G. Ankele, "Self-Imaging in Homogeneous Planar Optical Waveguides", *Applied Physics Letters*, **27**:6, (1975)
- [37] P. A. Besse, M. Bachmann, H. Melchior, L. B. Soldano and M. K. Smit, "Optical Bandwidth and Fabrication Tolerances of Multimode Interference Couplers", *Journal of Lightwave Technology*, **12**:6, (1994)
- [38] E. C. M. Pennings, R. J. Deri, A. Scherer, R. Bhat, T.R. Hayes, N. C. Andreadakis, M. K. Smith, L. B. Soldano and R. J. Hawkins, "Ultra-compact, Low-loss Directional Couplers on InP Based on Self-Imaging by Multimode Interference", *Applied Physics Letters*, **59**:16, (1991)

- [39] L. H. Speikman, Y. S. Oei, E. G. Metaal, F. H. Groen, I. Moerman, M. K. Smith, and B. H. Varbeek, "Extremely Small fabrication-tolerant InP-based Power Splitting and Combining Structures by Deep Etching", in Proc. European Conf. Opt. Commun.(ECOC), Firenze, Italy, Sept. (1994)
- [40] J. Fan, M. W. Geiss, and B-Y Tsaur, "Lateral Epitaxy by Seeded solidification for Growth of Single -Crystal Si Films", Applied Physics Letters, **38**:5, (1981)
- [41] S. K. Ghandhi, "VLSI Fabrication Principles, Silicon and gallium Arsenide", New York:John Wiley & Sons, (1994)
- [42] M. Bruel "Silicon on Insulator Material Technology ", Electronics Letters, **31**:14, (1995)
- [43] R. Williams, "Modern GaAs Processing Techniques", Nowood, MA:Artech Hauses Inc., (1990)
- [44] R. Wolf and R. N. Tauber, "Silicon Processing, Volume1-Process Technology", Sunset Beach, CA:Lattice Press, (1986)
- [45] K. E. Bean "Anisotropic Etching of Silicon", IEEE Transactions on Electron Devices, **ED-25**:10, (1978)
- [46] W-T Tsang, C-C Tseng, and Shyh Wang "Optical Waveguides Fabricated by Preferential Etching", Applied Optics, **14**:5, (1975)
- [47] J. Schmidchen, A. Splett, B. Schüppert, K. Petermann "Low Loss Singlemode Optical Waveguides with large Cross-Section in Silicon-on-insulator ", Electronics Letters, **27**:16, (1991)